Assessing Sensitivity of Subsurface Mine-Dewatering Activities to Climate Change

by

Adam Calvert

A thesis

presented to the University of Waterloo

in fulfillment of the

thesis requirement for the degree of

Master of Science

in

Earth Sciences

Waterloo, Ontario, Canada, 2023

© Adam Calvert 2023

Author's Declaration

I hereby declare that I am the sole author of this thesis. This is a true copy of the thesis, including any required final revisions, as accepted by my examiners. I understand that my thesis may be made electronically available to the public.

Abstract

Underground mining activities require constant removal of groundwater from their void spaces to maintain dry and safely accessible excavations for ore extraction in a process known as dewatering. The nature and degree of dewatering activities is heavily dependent on the amount of groundwater that can reach the mined areas and, conversely, dewatering of mines has a significant effect on the regional groundwater flow in their vicinity. Furthermore, groundwater supply to mining areas may be linked to climatic conditions, connected surface water bodies and the geologic structures that link the surface and subsurface. Typically, fully saturated groundwater models are used in industry to simulate site conditions and to plan mine dewatering infrastructure. These models often take historical climate averages into account when determining recharge to groundwater from the surface, and they do not typically account for feedback between groundwater and surface water systems. While this has been sufficiently accurate in the past, it is expected that the progression of climate change will yield future estimates of groundwater recharge that differ significantly from historical averages. These changes may be captured more accurately with fully coupled methods of simulating groundwater and surface water simultaneously in areas with large surface water bodies overlying aquifers, or in locations where geologic structures provide significant preferential pathways between the surface and subsurface.

Here, we explored the changes in predicted dewatering rates for a real mining property in Central Quebec when considering a typical, industry standard fully saturated groundwater model with historically averaged recharge and a fully integrated groundwater/surface water

model that incorporates results from future climate scenarios. The two models were constructed, parameterized, and calibrated for a site in Central Quebec. Simulations of underground mine dewatering were run with both models, and the predicted dewatering rates from each model were compared. Simulation results demonstrated that the fully integrated groundwater/surface water model with future climate yielded an estimated rate of dewatering that was approximately 2% higher than that predicted by the fully saturated groundwater model with historical climate averages.

Acknowledgments

First and foremost, I wish to thank my supervisor, Dr. Andrea Brookfield, for her unfailing kindness, patience, and support through the entirety of my master's program. Her guidance was instrumental in completing my research and growing leaps and bounds as a scientist but, in addition, her willingness to see my potential when it was not immediately apparent granted me the opportunity of a lifetime to pivot into a field that I am now immensely passionate about.

I also want to extend immense gratitude toward my supervisor during my time with BluMetric Environmental Inc., Dr. Ali Nowamooz. His knowledge of the field, and willingness to impart it, were inspiring. Furthermore, he demonstrated astounding patience and kindness in all endeavors. He never hesitated to go above and beyond to educate and support me, and always encouraged me towards the best choices for my personal and professional growth.

I would additionally like to thank all my other colleagues at BluMetric, particularly Dr. Francois Richard, Dr. Mariana Trindade, and Vincent Mlakar. Their support was invaluable for successfully navigating research and consulting simultaneously, which provided significant additional professional growth and support during my time as a student. I also wish to extend my thanks to Dave Blowes, who provided extremely valuable feedback as a member of my thesis committee, and the rest of my research group for their support, assistance and comradery throughout my graduate program.

I would like to extend sincere gratitude to Brayden McNeil, Killian Miller, Graham Stonebridge and the rest of the team at Aquanty Inc, who never failed to go above and beyond

in troubleshooting my many challenges with HydroGeoSphere. I would also like to thank Brock Norwood for his very helpful support with all things related to FEFLOW.

I would like to extend my sincere gratitude to my friends and family, particularly my mother and father and my partner Samantha. Their multitudes of support were a critical component of my success during my graduate studies and will undoubtedly continue to be a beacon in my most trying times going forward.

I wish to thank ClimateData.ca for providing the climate information used in this paper. ClimateData.ca was created through a collaboration between the Pacific Climate Impacts Consortium (PCIC), Ouranos Inc., the Prairie Climate Centre (PCC), Environment and Climate Change Canada (ECCC) Centre de Recherche Informatique de Montréal (CRIM) and Habitat7.

I also acknowledge the World Climate research Programme's Working Group on Coupled Modelling, which is responsible for CMIP, and I thank the climate modeling groups for producing and making available their model output. For CMIP, the U.S. Department of Energy's Program for Climate Model Diagnosis and Intercomparison provides coordinating support and led development of software infrastructure in partnership with the Global Organization for Earth System Science Portals.

In addition, I would like to thank and acknowledge the efforts of field technicians at BluMetric Environmental Inc. for the collection of field data used in this work – particularly the 8 packer tests conducted between November and December of 2021 and utilized in model parameterization.

Table of Contents

Author's Declaration ii

Abstract iii

Acknowledgments v

List of Figures ix

List of Tables xii

List of Equations xiii

1. Introduction 1

1.1. Scope and Research Objectives 3

1.2. Background 4

1.2.1. Numerical Modelling 4

1.2.2. Dewatering Simulation 6

1.2.3. Climate Change 7

2. Methods 9

2.1. Description of Study Site 9

2.1.1. Topography 10

2.1.2. Geology 11

2.1.3. Climate 15

2.1.4. Land Use and Cover 15

2.2. Model Development 16

2.2.1. Model Domain 17

2.2.2. Boundary Conditions 18

2.2.3. Parameterization of Hydraulic Conductivity 23

2.2.4. Numerical Grid Generation 25

2.2.5. Fracture, Fault and Gallery Representation 26

2.2.6. Sensitivity Analysis 27

2.2.7. Surface Parameters 28

2.3. Recharge, Climate and Evapotranspiration 28

3. Model Results 34
3.1. Base Case Simulations of Natural Conditions 35
3.2. Simulation of Dewatering in Underground Galleries 44
4. Discussion 54
4.1. Uncertainty 58
4.1.1. Uncertainties in Observational Data 62
5. Conclusions and Recommendations 65
References 67
Appendices 77
Appendix A: HydroGeoSphere Governing Equations 77
Appendix B: Recharge Equations 81
Appendix C: FEFLOW Governing Equations 91
Appendix D: Catchment Analysis 93
Appendix E: Packer Test Results 95
Appendix F: Location and Representation of Galleries 98
Appendix G: Summary of Simulation Results 100
Appendix H: Differences Between Common Node and Dual Node Scheme 101

List of Figures

Figure 2.1 - Location of Study Site Highlighting Mining Properties and Major Waterbodies 10

Figure 2.2 - Topographic Contour Map of Chibougamau Region 11

Figure 2.3 - Regional Geologic Structures of Chibougamau 12

Figure 2.4 - Chibougamau Regional Catchments 18

Figure 2.5 - Wells and Boreholes with Water Level Measurements 19

Figure 2-6 - Constant Head Boundaries Applied to the Model Surface to Represent Lakes 23

Figure 2-7 - Seepage Boundary Conditions Applied to Galleries 23

Figure 2-8 - Flux Boundary Conditions Applied to Bottom Surface of Model 23

Figure 2-9 - 3D Model Mesh – FEFLOW 26

Figure 3.1 - Results of FEFLOW Base Case Simulation - Steady-State Saturated without Calibration 36

Figure 3.2 - 3D Hydraulic Head Distribution of the Steady State Saturated Base Case Model in FEFLOW 37

Figure 3.3 - Results of HydroGeoSphere Base Case Simulation - Steady-State Saturated 38

Figure 3.4 - 3D Hydraulic Head Distribution of the Steady State Saturated Base Case Model in HydroGeoSphere 39

Figure 3.5 - Results of the HydroGeoSphere Base Case Simulation with Unsaturated Flow Conditions - Transient Run for 50 Years 41

Figure 3.6 - 3D Hydraulic Head Distribution of the Transient Unsaturated Base Case Model in HydroGeoSphere 42

Figure 3.7 - Results of the HydroGeoSphere Fully Coupled Groundwater/Surface Water Base Case Simulation - Transient Run for 50 Years 43
Figure 3.8 - 3D Hydraulic Head Distribution of the Fully Coupled Groundwater/Surface Water Base Case Model in HydroGeoSphere 44
Figure 3.9 - 2D (Surface) and 3D Hydraulic Head Distribution of the Steady State Saturated Dewatering Simulation in FEFLOW 45
Figure 3.10 - 2D Hydraulic Head Distribution of the a) Site A and b) Site B Mine Galleries in the Steady State Saturated Dewatering Simulation in FEFLOW 46
Figure 3.11 - 2D (Surface) and 3D Hydraulic Head Distribution of the Steady State Saturated Dewatering Simulation in HydroGeoSphere 48
Figure 3.12 - 2D (Surface) and 3D Hydraulic Head Distribution of the Fully Coupled Groundwater/Surface Water Dewatering Simulation with Historical Climate Forcing in HydroGeoSphere 50
Figure 3.13 - 2D (Surface) and 3D Hydraulic Head Distribution of the Fully Coupled Groundwater/Surface Water Dewatering Simulation with Future Climate Forcing in HydroGeoSphere 52
Figure 4.1 - Locations of Synthetic Pilot Points 55
Figure 4.2 - Hydraulic Head Correlation Between Synthetic Pilot Points in FEFLOW and HGS 55
Figure 4.3 - Trend in Net Recharge Over Time Applied as Climate Forcing for the Fully Coupled Transient HGS Dewatering Model 57
Figure 4.4 - Differences in Fracture/Matrix Interaction Between Dual Node and Common Node Scheme 60

Figure A.1 - General Landforms Identified Across Study Site 83

Figure A.2 - Percent Slope Calculated Across Study Site 84

Figure A.3 - Estimated Slope Coefficient Across Study Site 85

Figure A.4 - Vegetation Factor Across Study Site 86

Figure A.5 - Soil Moisture Storage Coefficient Across Study Site 87

Figure A.6 - Calculated Recharge Coefficient Across Study Site 88

Figure A.7 - Location of Packer Testing Boreholes 95

Figure A.8 - Packer Testing Results (From Top to Bottom – CDB-FE3-21, CDB-18-03 (768m Interval), CDB-18-03 (499m Interval), CDB-20-04) 96

Figure A.9 - Packer Testing Results (From Top to Bottom – CDB-FE4-21 (56m Interval), CDB-FE4-21 (29m Interval), CDB-FE5-21 (77m Interval), CDB-FE5-21 (26m Interval)) 97

List of Tables

Table 2.1 - Legend for Figure 3 13

Table 2.2 - Observation Points in Site A and Site B 20

Table 2.3 - Summary of Boundary Conditions in Steady-State Saturated Model 22

Table 2.4 - Summary of Packer Tests 25

Table 2.5 - Model Land Classes with Matching NLCD Land Classes and Associated Manning Coefficients 28

Table 3.1 – Rate Budgets for FEFLOW and HGS Steady State Saturated Base Case Models 39

Table 3.2 – Summary of Water Balance Results for Dewatering Models 47

Table 3.3 - Summary of Dewatering Rates 53

Table A.1 - Collective Simulation Results of All Base Case Scenarios 100

Table A.2 - Summary of Dewatering Rates 101

List of Equations

Equation 2.1 – Calculation of Surface Runoff in millimetres per year 31

Equation 2.2 - Calculation of Historical Groundwater Recharge 31

Equation A.1 - 2D Diffusive Wave Equation 77

Equation A.2 - Coupling Momentum with the 2D Saint Venant Equation 78

Equation A.3 - Richard's Equation 78

Equation A.4 - Dual Node Exchange Flux 79

Equation A.5 - Manning Equation 80

Equation A.6 - Potential Evapotranspiration 81

Equation A.7 - Runoff Volume 82

Equation A.8 - Runoff Coefficient 82

Equation A.9 - Recharge 88

Equation A.10 - Hargreaves Samani Estimate of ET 89

Equation A.11 - Darcy's Law 91

1. Introduction

Mining operations are critical to the mass extraction and utilization of economically significant mineral resources known as ores, which typically form deep in the Earth's subsurface along physically and chemically active geologic structures (Jenkin et. al, 2014). Ores must be dug or blasted from their host rock to be transported, refined, and eventually utilized in the production of goods. Accessing these deep ore bodies requires mining companies to either excavate massive pits that are open to the surface and extend deep into the ground, known as open pit mining, or dig out large horizontal underground tunnels, known as galleries, that are vertically connected and accessed from the surface via a series of elevator shafts, known as underground mining (Mousavi & Sellers, 2019). In either case, the commonality is that these deep underground excavations directly impact regional groundwater flow system by displacing and altering the structure of aquifer materials, which in turn may alter preferential pathways and available storage (Blodgett & Kuipers, 2002).

Without an engineered intervention these underground excavations may be constantly saturated with groundwater, provided the lower bounds of excavation are below the water table, making ore extraction extremely difficult and unsafe while contributing significant contamination to local aquifers (Blodgett & Kuipers, 2002). As such, keeping open pits and underground galleries constantly dry is essential to the safe and economically effective operation of a mine. This is achieved by continuously pumping out the groundwater and surface water inflows reaching these excavations to a suitable location in a process known as dewatering.

Mining operations typically occur on large scales that result in excavations naturally receiving significant volumes of groundwater inflow that necessitate large pumping rates to effectively keep them dry (Blodgett & Kuipers, 2002). The pumping infrastructure required to meet this demand is often complicated and expensive in terms of acquisition, setup, operation and maintenance. Furthermore, the financial, safety and environmental impacts of improperly designing a dewatering system are too costly to leave to trial and error (Cahyadi et. al, 2020). These problems are further complicated as the natural groundwater flow regime and dewatering requirements of the mine will change as new excavations are made and the mine evolves over its lifespan. As such, effective mining operations demand a precise, scalable, and cost-effective tool for estimating groundwater inflows to their workings and the needed pumping infrastructure and dewatering rates (Hu et. al, 2020).

Numerical groundwater modelling has proven to be a highly effective tool to meet these needs, allowing mine operators to create digital simulations of their properties that can predict current and future groundwater flow conditions and provide an environment for testing dewatering strategies and receiving direct feedback without immediately investing in costly pumping infrastructure (Hu et. al, 2020). Traditionally, this has been done throughout the industry using more traditional numerical modelling packages such as MODFLOW and FEFLOW, which simulate only the groundwater component of the hydrologic cycle and incorporate surface water as simplistic boundary conditions that do not interact dynamically with groundwater in the model (Szczepiński, 2019).

Recent research in numerical hydrologic modelling has demonstrated that interactions and feedback mechanisms between surface water and groundwater systems are a critical aspect of groundwater flow regimes, and that fully coupling groundwater and surface water components to yield dynamic interactions at the scale of the watershed has observable influences on simulated flow regimes that are not captured by simplistic groundwater only models (Kollet & Maxwell, 2006). This becomes especially relevant when predicted changes in climate from global climate models are accounted for in the recharge component of the simulation. Future changes in climate are anticipated to have a major impact on surface and subsurface hydrology (Goderniaux et. al, 2009). Presently, these influences are not widely considered in the context of dewatering plans for future mining operations, which often utilize models based on groundwater only representations and historical climate averages (Earman & Dettinger, 2011). These simplistic models will likely prove to be less predictable over time as climate continues to deviate from historic averages. This thesis aims to explore the applicability of fully integrated groundwater/surface water modelling methods with climate forcing in the context of mine dewatering operations.

1.1. Scope and Research Objectives

The primary research objective is to evaluate the robustness of current industry standard numerical modelling methods in predicting groundwater storage and dewatering volumes for underground mining projects when future variations in climate are accounted for. Further to this, direct comparisons will be explored between predictions from groundwater-exclusive modelling methods and fully integrated hydrologic models. The conclusions drawn

from these comparisons will provide insight into the future applicability of current modelling methods relative to anticipated changes in climate, and the potential necessity of adopting more complex models that represent the entirety of a watershed and the terrestrial hydrologic system.

The scope of this thesis will include the development and parameterization of a conceptual model, a numerical groundwater model, and a fully integrated numerical groundwater/surface water model, as well as the application of both historical climate data and a future forecasting climate model to the numerical models. Simulations with both historical and future climate data sets will be run, and the resulting volumetric flow in each model (calculated as a rate budget) will be analyzed and compared.

1.2. Background

Significant research efforts have been dedicated to the practice of numerical groundwater modelling and its applications in mine dewatering and climate contexts. However, a review of relevant literature as outlined below demonstrates that few studies to date have explored the explicit dynamics between climate change, mine dewatering simulation and full-scale watershed modelling.

1.2.1. Numerical Modelling

Numerical models have been utilized as tools for understanding groundwater systems as early as the mid 1960's (Freeze and Witherspoon, 1966). As larger and more complex domains were considered, these early analytical models evolved into the computationally driven modelling packages we use today like the finite-difference based MODFLOW (McDonald &

Harbaugh, 1984; Langevin et. al, 2017) and finite-element based FEFLOW (DHI Group, 2022). These packages lack inherent integration of surface water flow, typically utilizing simple recharge boundary conditions or, in more advanced use cases, loose coupling of the boundary conditions with recharge predicted in separate surface water simulations (DHI Group, 2022).

While the earliest attempts at unifying principles of groundwater and surface water flow date back to the late 1960's (Freeze & Harlen, 1969), with some important studies that expand on those principals to explore the behaviour of the transition zone between groundwater and surface water (Winter, 1978), it is not until recently that several new tools have been developed with the aim of tackling fully integrated groundwater/surface water numerical modelling, with varied hydrological applications such as cold regions hydrology (Yang et. al, 2021), continental scale hydrologic predictions (Chen et. al, 2019) and fully integrated coastal modelling (Lou et. al, 2018). This is typically accomplished through coupling of the 2D Saint Venant Equation for surface flow and Richard's equation for variably saturated flow in 3D via an exchange flux term (further expanded upon in Appendix I). GSFLOW, built by the USGS, draws on their previous groundwater modelling framework, MODFLOW (Markstrom et. al, 2008), and surface water modelling framework, the Precipitation-Runoff Modelling System or PRMS-V (Markstrom et. al, 2015), to create a tool that fully couples groundwater and surface water and simulates the entire watershed simultaneously. Similarly, ParFlow is an open-source, fully coupled groundwater/surface water simulation framework with capabilities for incorporating complex evapotranspiration and snow-cover processes and scalability for high-power computing (Kollet & Maxwell, 2006). HydroGeoSphere (HGS), developed by Aquanty Inc.,

provides a comprehensive modeling environment for fully integrated groundwater/surface water simulations incorporating all the features of both ParFlow and GSFLOW with additional features such as variable-density flow, heat transport, reactive chemical species transport and first order decay reactions (Brunner & Simmons, 2011).

1.2.2. Dewatering Simulation

Rapantova et. al (2007) addresses some common considerations that must be applied to numerical models of mines, including the need for accurate representation of fractures, dual porosity flow and leakage through rock matrices. However, no mention is made of integrating surface water processes. Szczepiński (2019) provides further insight on groundwater modelling for mining applications but focuses primarily on traditional groundwater modelling methods with no consideration for integrating surface water interactions, explicitly mentioning that numerical models developed for mine sites typically incorporate surface water recharge as first or third type boundary conditions.

Prior studies have demonstrated that lakes connected to subsurface fracture networks can have a significant influence on the hydrologic conditions in underground mine workings and that there is a need to consider surface water components to improve dewatering estimates in traditional groundwater models (Mu et. al, 2018). Other studies exploring the connection between lakes and underground mining galleries have not always found an explicit connection but have generally determined that considering surface water bodies had an influence on some important aspect of the local aquifer, and that more observations over time may demonstrate more explicit linkage (Dong et. al, 2014).

Groundwater modelling studies of a very similar nature to the simulations undertaken in this thesis – including fracture flow, underground mining voids and dewatering – have typically only incorporated recharge from meteoric water as a transient boundary condition at the surface of the model (Dong et. al, 2012), or as a constant recharge determined as a percentage of calculated surfacewater runoff from historically average precipitation (Hu et. al, 2020).

1.2.3. Climate Change

While there appears to be almost no studies that explicitly incorporate climate change factors and fully integrated hydrologic modelling in the context of mining operations, there are numerous informative publications outside the context of the mining industry that explore hydrologic modelling with climate change scenarios. Most studies tend to employ one of various global climate models when formulating their respective climate change scenarios. Incorporating transient changes in climate parameters (precipitation, evapotranspiration, etc.) predicted by global climate models is known as climate forcing.

Studies exploring the link between groundwater availability and climate change induced variations in precipitation through numerical groundwater modelling have demonstrated direct links between future reductions in precipitation predicted by global climate models and a decrease in groundwater availability (Lam et. al, 2021). Comparable groundwater modelling studies have also demonstrated direct links between increases in precipitation predicted by global climate models and increases in groundwater recharge (Appiah-Adjei, 2006). These relationships, and similar direct relationships between groundwater/surface water availability and climate-induced changes in evapotranspiration, have also been demonstrated in the

context fully integrated groundwater/surface water models (Cochand et. al, 2019). Even in studies that note only minor variances in groundwater storage associated with climate forcing, major variances are note when interactions between aquifers and local river systems are considered (Scibek & Allen, 2006). In studies that consider fully coupling of groundwater and surface water components, climate has been shown to be the most significant factor impacting regional water balance (Van Roosmalen et al., 2009).

Numerous global climate models are available and may be used in studies of variation in groundwater recharge. In all cases, global climate models are often low-resolution and large (kilometer) scale and must be altered to provide results on a finer, more localized scale for the study area in question. This process is known as downscaling and there are numerous statistical methods that may be used to achieve it. Previous studies of a similar nature to this one utilized various version of the Canadian Global Climate Model and the delta-change statistical downscaling method to derive localized future climate datasets (Hashemi et. al, 2015).

With the current state of research in hydrologic modelling, climate integration and applications to dewatering simulation summarize above, the following chapters will outline the methods used to parameterize the dewatering simulations in this thesis (Chapter 2), the results of those simulations and how they compare to each other (Chapter 3), and a discussion of the modelling results and uncertainty (Chapter 4).

2. Methods

To adequately compare mine dewatering predictions between groundwater models and fully integrated groundwater/surface water models, a conceptual model of the study site must first be constructed, followed by the development and calibration of the numerical groundwater model and additional parameterization of surface water components for the integrated model.

2.1. Description of Study Site

The study site consists of two mining properties in the Nord-du-Quebec region of Central Quebec – Site A and Site B – that align on a bearing of approximately N80°W on opposite banks of the large body of water, Lac Dore (Figure 2.1). Both sites host historically exploited underground mining galleries which intersect a complex regional network of faults, shears and fractures. The commercial entities interested in these properties intend to continue extraction from these historic galleries at greater depths, where exploration has revealed additional mineralization deeper in the shear zones. The town of Chibougamau (2021 population: 7,233) is located approximately five kilometres to the east of the study site (Statistics Canada, 2023).

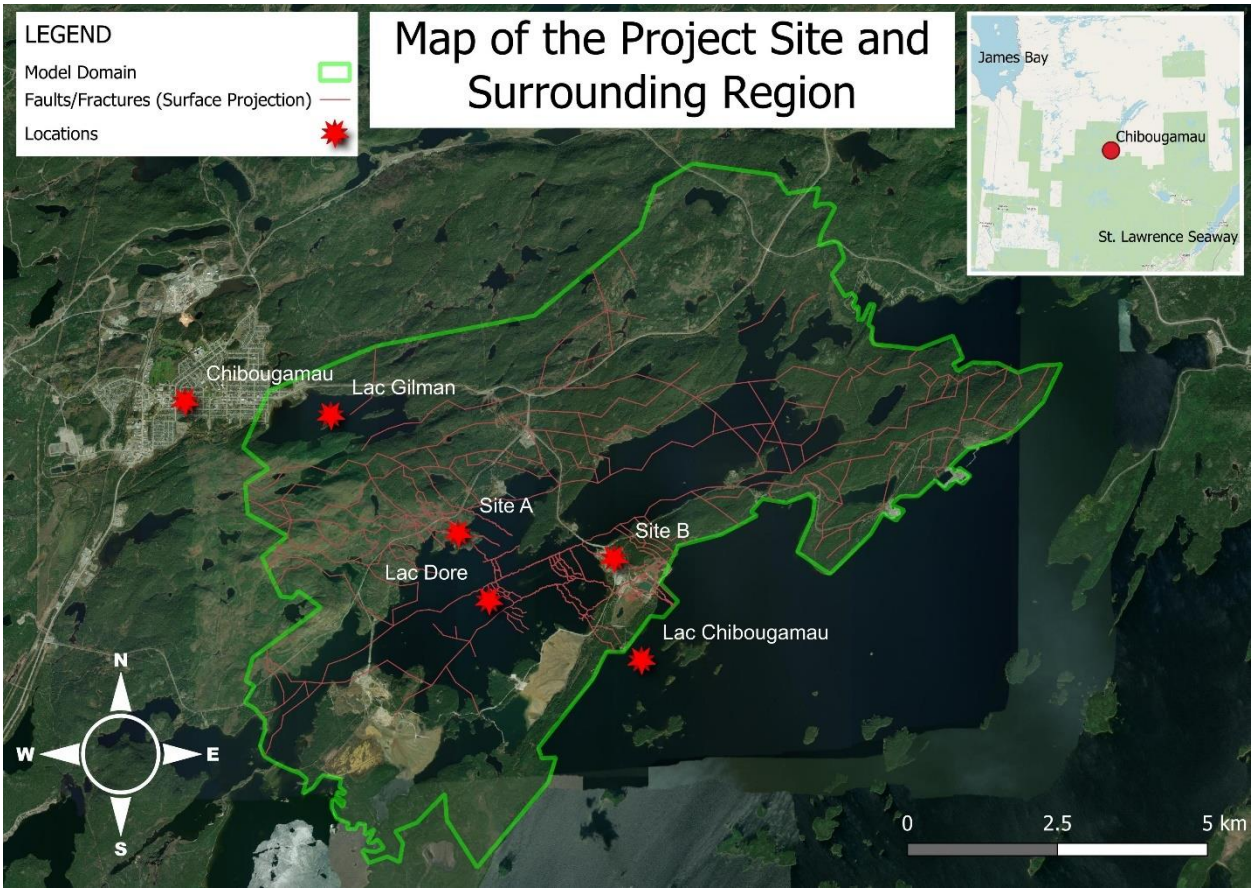


Figure 2.1 - Location of Study Site Highlighting Mining Properties and Major Waterbodies (Basemap modified from ESRI Satellite World Imagery, Faults and Fractures modified from Leclerc et. al, (2017))

2.1.1. Topography

The landscape of the study site is characteristic of the Laurentian Mountains with hilly, rolling terrain. Elevation difference within the study area is nearly 164 m between the lowest point at the surface of Lac Dore (376 masl) and the highest point in the mountains to the North of the lake (540 masl), which separate it from Lac Gilman and the Township of Chibougamau (Figure 2.2). Lac Dore itself spans the middle of the study site, separated from a larger upstream lake, Lac Chibougamau, by the mountainous Gouin Peninsula where Site B is located. Surficial

terrain varies considerably between exposed bedrock, glacial till, peaty wetlands, and densely forested areas.

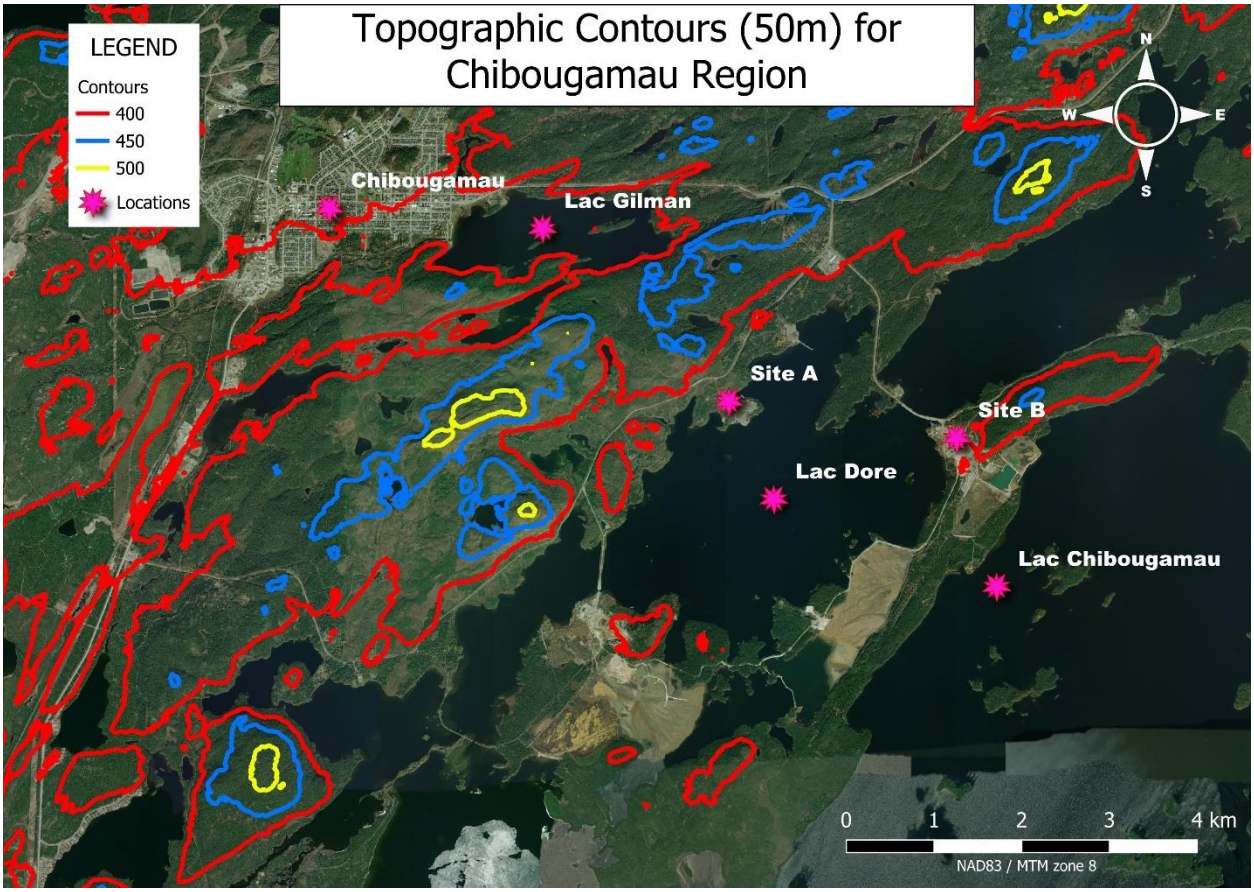


Figure 2.2 - Topographic Contour Map of Chibougamau Region (Basemap modified from ESRI Satellite World Imagery)

2.1.2. Geology

The local geology of the study site resides on the Northern flank of the Chibougamau Anticline, where regional deformation has exposed lower bedrock units near surface (Evans, 2019). While a thin layer (<20 m) of what is likely Opemisca Group glacial till can be found discontinuously at the surface, most surface deposits are comprised of synvolcanic Roy Group

geologic materials (Daigneault & Allard, 1990). Blondeau formation volcanoclastic materials are primarily evident directly at the surface, confined a few tens of meters below by Cummings Group Sills of Gabbroic rock (Daigneault & Allard, 1990). Gilman formation rocks underly the sills, consisting mainly of mafic volcanic rocks that in some cases have little distinction from the gabbroic anorthosite of the Lac Dore Complex (LDC) and intruding Chibougamau Pluton, which further underly the Gilman formation and are extensive from a 2500 m contact point to as far as 3600 m below the surface throughout the region (Daigneault & Allard, 1990). Due to regional tectonic history and the location the study site on the Chibougamau Anticline, LDC gabbroic anorthosites may be found much closer to the surface in the borehole records. The stratigraphic record is visualized in Figure 2.3, with legend information provided in Table 2.1.

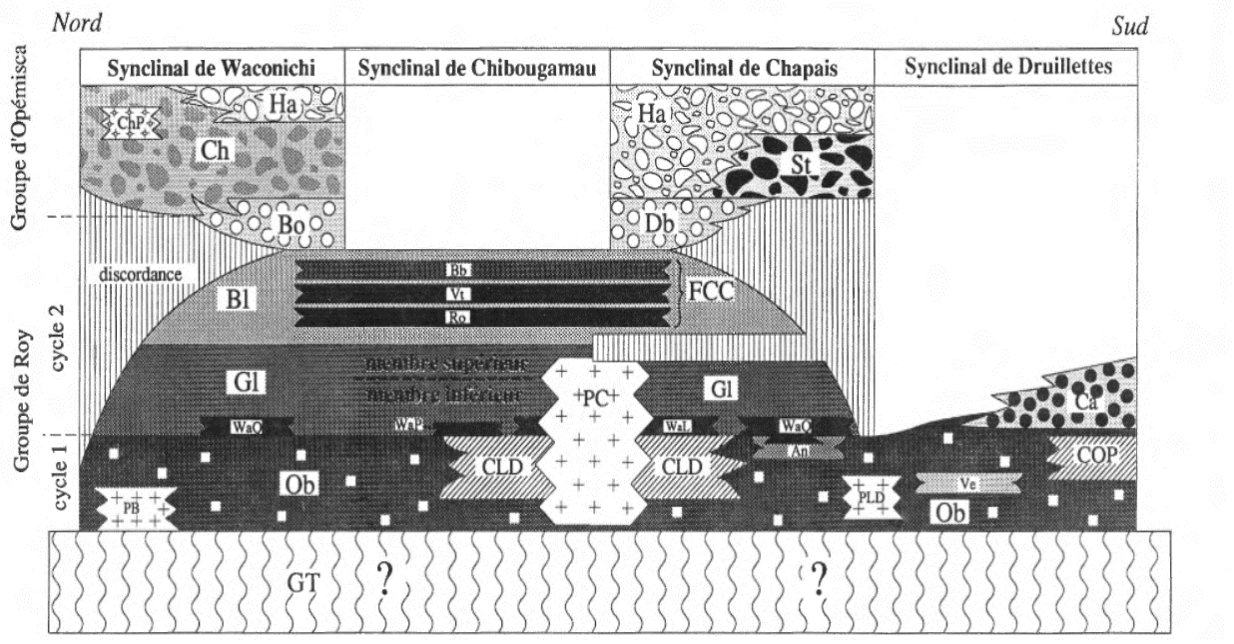


Figure 2.3 - Regional Geologic Structures of Chibougamau (Modified from Daigneault & Allard, 1990)

Table 2.1 - Legend for Figure 3

<table>
<tr><th colspan="4">LEGEND</th></tr>
<tr><th>Formations</th><th>Complexes</th><th>Suites</th><th>Plutons</th></tr>
<tr>
<td rowspan="2">Ha – Hauy Formation
Ch – Chebistuan Formation
Bo – Bordeleau Formation
Bl – Blondeau Formation
Gl – Gilman Formation
St – Stella Formation
Ob – Obatagamau Formation
Ca – Caopatina Formation
Db – Daubree Formation</td>
<td>CLD – Lac Dore Complex
COP – Opawica Complex</td>
<td rowspan="2">FCC – Cummings Intrusive Suite
Bb – Bourbeau Intrusion
Vt – Ventures Intrusion
Ro – Roberge Intrusion

Wa – Waconichi Formation
WaQ – Queylus Type
WaL – Lemoine Type
WaP – Portage Type</td>
<td rowspan="2">PLD – Dauversiere Pluton
PCh – Chevrillon Pluton
PB – Barlow Pluton
PC – Chibougamau Pluton</td>
</tr>
<tr>
<td>Members
An – Andy Member
Ve – Vents Member
GT – Tonalitic Gneiss</td>
</tr>
</table>

The matrix of gabbroic anorthosite encompassing most of these units is punctuated with an extensive and complex regional network of faults, fractures, and shear zones owing to the lithology's long and multifaceted history of tectonic alteration. Shear zones in the study site extend tens to hundreds of meters along their 120° Northwest-Southeast strike, dipping steeply Northeast with an average width of 1.5 m (Evans, 2019). It is within these shear zones that economic mineralization primarily occurs. Diabase dykes tend to bound mineralization zones in both Site A and Site B (Evans, 2019). These shear zones connect to, and are connected by, the massive Lac Dore Fault which strikes Northeast directly through the middle of its namesake lake and transects the underground galleries of both mining properties. The Lac Dore Fault has a variable dip of 50 to 70 to the Northwest, and a significant dextral strike-slip displacement of 1600 m which owes to the truncation and horizontal displacement of various shear zones (Evans, 2019; RadonEx Ltd., 2011). Additional minor faults, likely of the same tectonic origin,

may be found north and south of the Lac Dore Fault, with approximately equivalent strikes and dips (Leclerc et. Al, 2017). Surface projections of the faults are shown in Figure 1.

To the North of Lac Dore, another major regional fault known as the Lac Sauvage Fault spans the study site, striking Northwest and terminating in a connection with the Lac Dore fault at the eastern terminus of Lac Dore (Leclerc et. Al, 2017). Little information is available accounting for the dip, depth, or width of the Lac Sauvage Fault due to its highly variable and discontinuous nature making it a challenge to study in the field (Daigneault & Allard, 1990). However, what information can be inferred from exposures suggests that it is a steeply dipping thrust fault that yields local repetition of certain displaced stratigraphic units along its strike (Daigneault & Allard, 1990).

Additional minor faults striking north to south are interspersed throughout the region, branching off both the Lac Dore Fault and Lac Gilman fault and, in some areas, bridging these two major regional structures (Leclerc et. al, 2017). It appears evident that regional faulting and shearing occurred after the formation of Roy Group rocks (Daigneault & Allard, 1990). In addition, it is mentioned that the Lac Dore fault is likely present (but submerged) along the entirety of Lac Dore, with brief exposures on land at either end to the East and West (Daigneault & Allard, 1990). Furthermore, economic mineralization, associated with shear zones in the region, appears to be prevalent to the lowest depths of the Lac Dore Complex (RadonEx Ltd., 2011). Thus, an assumption can be made that regional fault structures are vertically extensive from surface to depth.

2.1.3. Climate

Despite residing just slightly south of 50°N, the region surrounding Chibougamau has a Köppen–Geiger Climate Classification of Dfc, correspondent with a continental subarctic climate displaying no discernible dry season and relatively cold summers (Beck et. al, 2018). This is evident in its historical climate statistics, which average 941 mm/annum of precipitation (of which approximately 1/3rd is snowfall not converted to snow water equivalent) and a mean annual summer temperature of 15.1 °C (Prairie Climate Centre, 2019). Evapotranspiration (ET) throughout the region averages 457 mm/annum (Prairie Climate Centre, 2019).

2.1.4. Land Use and Cover

Land cover in the Chibougamau region is a mix between lightly vegetated tundra with shrubs, grasses and mosses, boreal forest and disturbed barren land from previous mining operations scattered throughout the area (represented in Figure A.1 in Appendix II). The landscape is interspersed with numerous large and small water bodies and relatively few interconnecting streams.

2.2. Model Development

Model development begins with a steady state saturated groundwater model (FEFLOW and HGS), followed by the additional parameterization of unsaturated soil parameters to create an unsaturated groundwater model (HGS) and finally, the addition of surface parameters to create a fully coupled groundwater/surface water model (HGS).

The initial steady state saturated groundwater model of the study site was developed using FEFLOW 7.5 (DHI, 2022). FEFLOW employs Richards' equation for saturated and unsaturated flow using finite element methods. Fractures may be represented in FEFLOW as discrete linear elements with distinct hydraulic conductivity that are coupled to the same matrix by either the same node (common node scheme) or by a two-node representation separated by a coupling length (dual node scheme) (DHI Group, 2022). This capability is critical to groundwater modelling in fractured rock massifs, as is common in mining applications, and separates FEFLOW from alternative modelling tools such as MODFLOW which, with the base package, are lacking in their capability to represent dual porosity flow systems (Rapantova et. al, 2007). Governing equations for FEFLOW are provided in Appendix III.

The fully integrated groundwater/surface water model was developed using HGS (Aquanty, 2018), which allows for incorporation of all elements of the groundwater model developed in FEFLOW with full coupling of surface water elements. The fully integrated model is a transient representation governed by unsaturated flow in the subsurface, with surface flow defined by the 2D depth-integrated diffusive wave version of the St. Venant equation for

surface water flow (Aquanty, 2018) and coupled through a first-order exchange flux term. Governing Equations for fully integrated groundwater/surface water flow are detailed in Appendix I.

2.2.1. Model Domain

The 2D surface extent of the model domain is determined by the boundaries of surface water bodies in the study area and their catchments – specifically the catchments of Lac Dore and Lac Gilman, and the northwestern border of Lac Chibougamau (Figure 2.4). Lac Gilman is incorporated despite its distance from the area of interest as initial simulations indicated that it may be within the zone of influence when dewatering the galleries. Catchment analysis is conducted in a process outlined by Hans van der Kwast (2021) using QGIS (QGIS.org, 2022) with algorithms from the PCRasterTools plugin (Karssenberg et. al, 2010) and digital elevation models (DEMs) sourced from the Government of Québec's Forêt Ouverte spatial database portal (Ministère des Forêts, de la Faune et des Parcs, 2019; Appendix IV). The vertical extent of the model was determined from information available in the deepest borehole logs for the region.

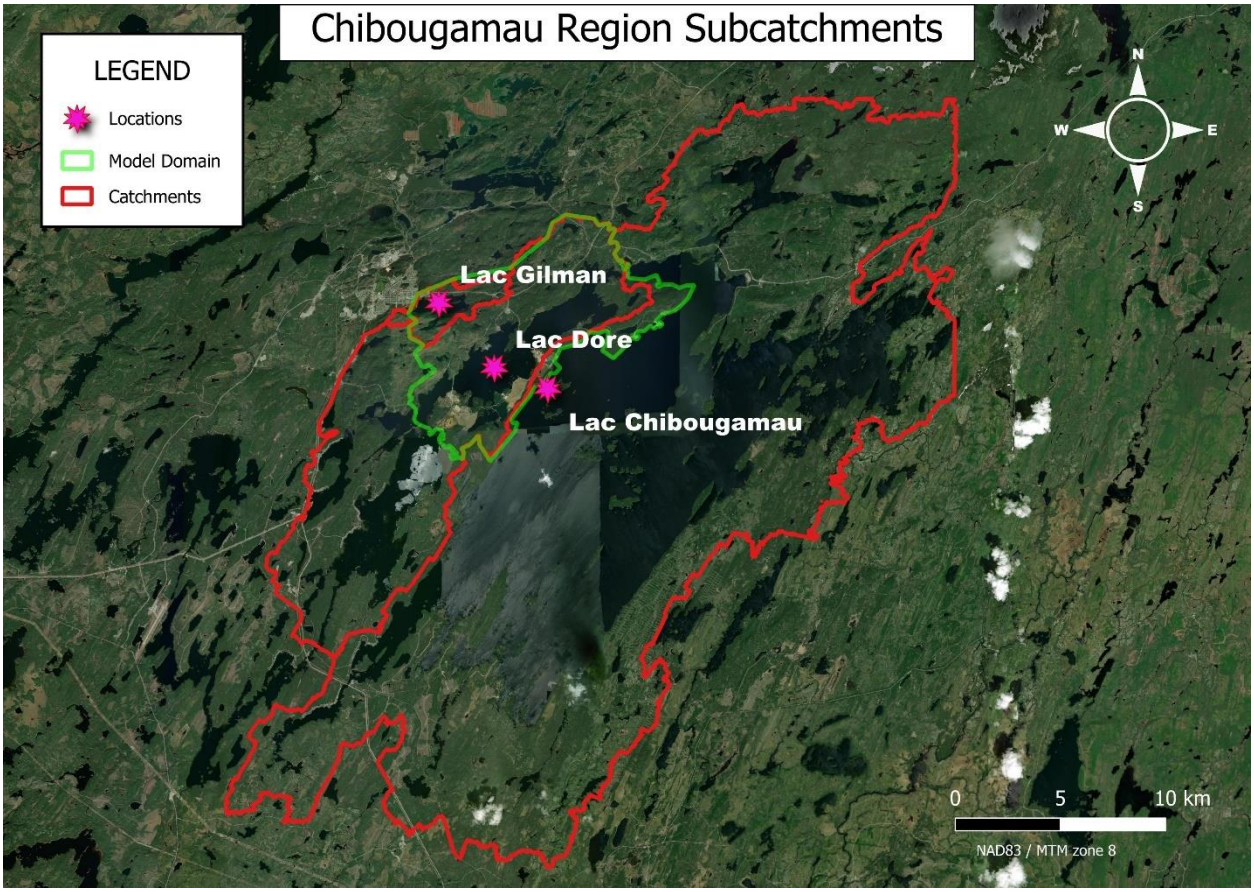


Figure 2.4 - Chibougamau Regional Catchments (Basemap modified from ESRI Satellite World Imagery)

2.2.2. Boundary Conditions

Flow primarily occurs through the fracture networks across the site which are exposed to the surface, yielding an unconfined aquifer system. Regional groundwater flow was determined to inform boundary conditions for the model by synthesizing the hydraulic head information available from wells and boreholes in the study area (Figure 2.5; Table 2.2), as well as the water levels of major lakes in the area and their inflows and outflows. Note that there is considerable uncertainty in the observed head data, related primarily to the spatial and

temporal resolution, which is discussed further in Section 4.1.1. As such, the observation heads used to calibrate the model represent an interpretation of the data with the best available information at the time of model construction but may be improved upon in the future with additional information. Groundwater flow in the region appears to be generally towards Lac Dore from the Northwest and Southeast.

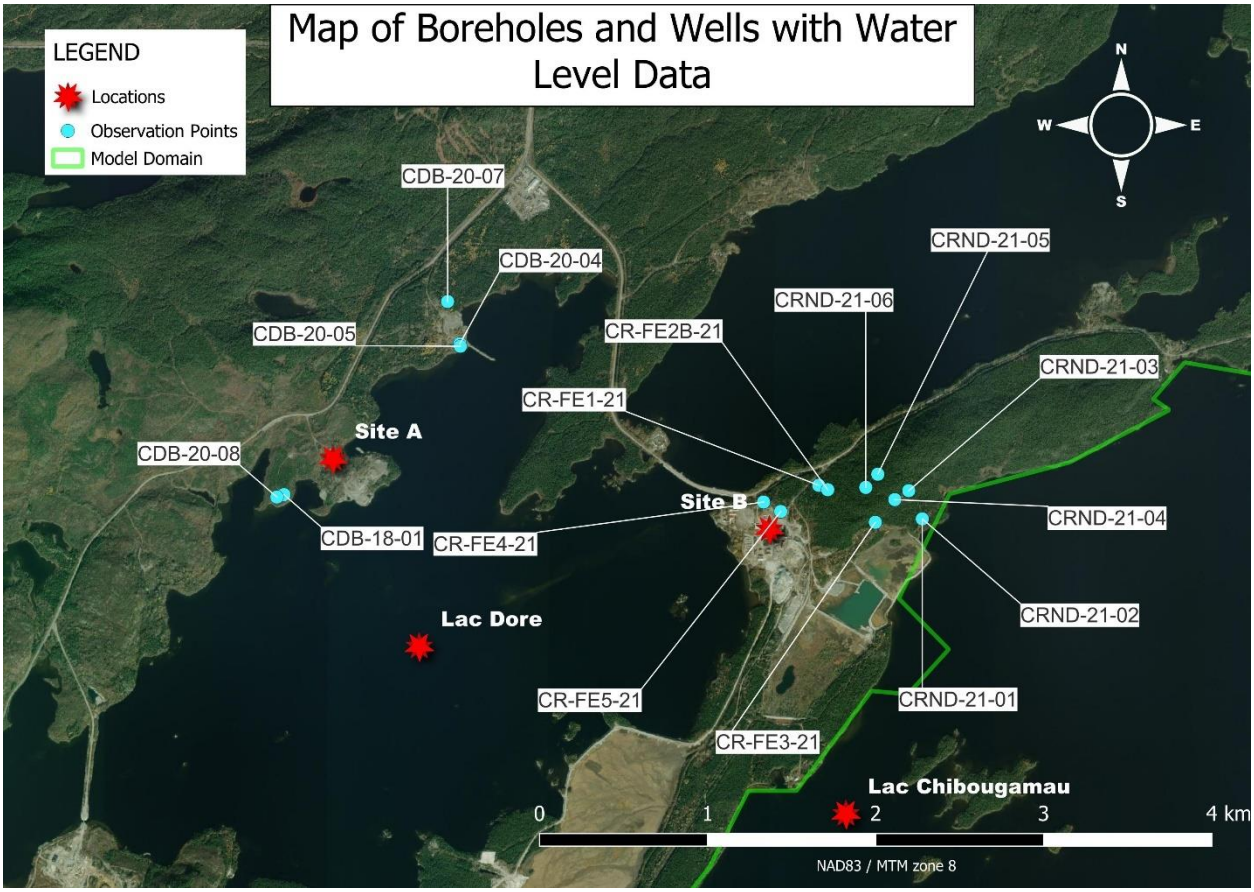


Figure 2.5 - Wells and Boreholes with Water Level Measurements (Basemap modified from ESRI Satellite World Imagery)

Table 2.2 - Observation Points in Site A and Site B

Site A/Site B Observation Points		
Well/Borehole	**Water Level (masl)**	**Approximate Date**
CDB-18-01	381.58	June 2021
CDB-20-04	379.74	June 2021
CDB-20-05	378.5	June 2021
CDB-20-07	380.44	June 2021
CDB-20-08	379.19	June 2021
CRND-21-01	385.4	June 2021
CRND-21-03	412.21	June 2021
CRND-21-04	415.77	June 2021
CRND-21-05	417.29	June 2021
CRND-21-06	412.08	June 2021
CR-FE1-21	385.61	August 2022
CR-FE2B-21	385.555	August 2022
CR-FE3-21	402.48	August 2022
CR-FE4-21	376.73	August 2022
CR-FE5-21	387.23	August 2022

Several boundary conditions are necessary to accurately model the site conditions (Table 2.3). For the groundwater only models, the nodes representing the three major waterbodies in the study area are assigned as constant head boundaries with values equal to the elevation of each lake's surface at the top slice of the model. A constant flux boundary condition equivalent to the vertical hydraulic conductivity at the lowest depth is applied to the entire bottom layer of the model domain to allow for outflow/drainage at the bottom of the domain. Note that due to differences in how FEFLOW and HGS represent inflow and outflow each model required a different sign convention to yield outflow out of the bottom. All remaining areas of the model with unassigned boundary conditions are treated as no flow boundaries.

When surface flow is incorporated in the model, the DEM defining the model topography is modified to include physical representation of the average basin depth for Lac Dore and Lac Gilman to allow HGS to accumulate surface water in these depressions. Lac Chibougamau's bathymetry was not incorporated as the model only touches its Northern boundary. Average basin depth was determined by extraction and averaging of contour values from an online bathymetric dataset that was available only for visualization and not download (GPS Nautical Charts, 2022). Furthermore, the fully integrated groundwater/surface water model requires an additional critical depth boundary around the perimeter of the surface of the model to allow surface runoff reaching the outer edges of the model to flow out of the domain.

Typically, integrating surface water flow in HGS would require removal of the constant head boundaries from the lakes to allow for simulation of changes to the lake levels. However, this would require that the entirety of the lake surfaces be incorporated into the numerical model, which was simply not possible due to the large size of Lac Dore and Lac Chibougamau and the computational complexity of simulating such a large domain. As such, constant heads were maintained for all models. Constant heads may be justifiable for the large lakes in this region relative to anticipated dewatering rates. For example, even considering a maximum dewatering rate estimate with common node fracture implementation of approximately 100,000 m^3/day, this would represent only 0.025% daily loss of Lac Chibougamau's estimated volume (~400,000,000 m^3).

When dewatering is applied to the simulation, the nodes corresponding to locations of the galleries are assigned a seepage boundary condition in FEFLOW, which combines a constant

head boundary equal to the elevation of the node and a maximum flux constraint of 0 L^3/t inflow, ensuring that water always flows out of the boundary and the galleries remain empty during the simulation. In HGS, this is represented equivalently with a constant head boundary equal to gallery elevation.

All boundary conditions are summarized in Table 2.3, and groundwater boundary conditions are visualized in Figure 2.6 (Constant Heads), Figure 2.7 (Gallery Seepage), and Figure 2.8 (Bottom Outflow).

Table 2.3 - Summary of Boundary Conditions in Steady-State Saturated Model

Summary of Boundary Conditions			
Boundary Description	Boundary Condition	Value	Model
Lac Dore	Constant Head (1st Type)	376 m	FSSG, FSSGD, HSSG, HSSGD, HUTG, HFCTG, HFCTG+
Lac Chibougamau	Constant Head (1st Type)	379 m	FSSG, FSSGD, HSSG, HSSGD, HUTG, HFCTG, HFCTG+
Lac Gilman	Constant Head (1st Type)	394 m	FSSG, FSSGD, HSSG, HSSGD, HUTG, HFCT, HFCT+
Outflow on Bottom of Domain	Constant Flux (2nd Type)	1e-08 m/s	FSSG, FSSGD, HSSG, HSSGD, HUTG, HFCT, HFCT+
Constant Recharge	Constant Flux (2nd Type)	42 mm/year	FSSG, FSSGD, HSSG, HSSGD, HUTG, HFCT
Recharge - Transient Climate Forcing	Constant Flux (2nd Type)	CMIP5 RCP 8.5 Precipitation – Hargreave-Samani ET	HFCT+
Site A Underground Galleries	Seepage	-398m to -498m	FSSGD, HSSGD, HFCT+
Site B Underground Galleries	Seepage	-698m to -798m	FSSGD, HSSGD, HFCT+
Surface Outer Perimeter	Critical Depth	N/A	HFCT, HFCT+

Model Key:	
FEFLOW – Steady State Saturated Groundwater	FSSG
FEFLOW – Steady State Saturated Groundwater with Dewatering	FSSGD
HGS – Steady State Saturated Groundwater	HSSG
HGS – Steady State Saturated Groundwater with Dewatering	HSSGD
HGS – Unsaturated Transient Groundwater	HUTG
HGS – Fully Coupled Transient Groundwater/Surface Water	HFCT
HGS – Fully Coupled Transient Groundwater/Surface Water with Dewatering and Climate Forcing	HFCT+

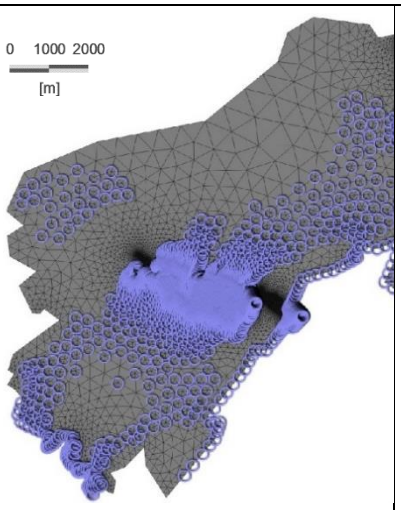


Figure 2-6 - Constant Head Boundaries Applied to the Model Surface to Represent Lakes

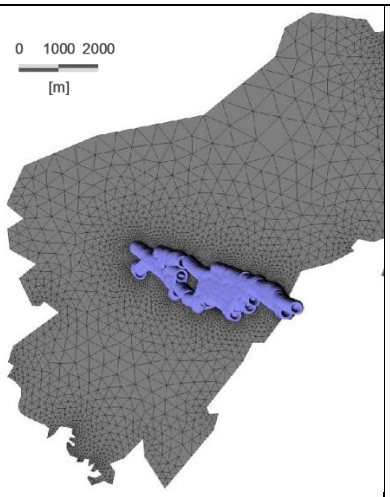


Figure 2-7 - Seepage Boundary Conditions Applied to Galleries

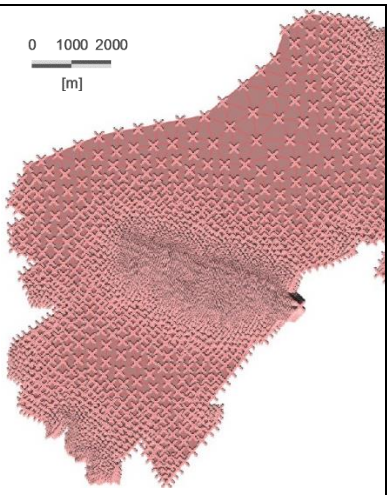


Figure 2-8 - Flux Boundary Conditions Applied to Bottom Surface of Model

2.2.3. Parameterization of Hydraulic Conductivity

Hydraulic conductivity of the matrix material and fractures was determined via analysis 8 of packer tests conducted in six wells around Site A using AquiferTest Pro 11 software (Waterloo Hydrogeologic, 2016), at depths ranging from 73 metres below ground surface (mbgs) to 1689 mbgs (Table 2.4). Locations and analytical results are visualized in Appendix V.

Three of the test wells showed anomalously high conductivity in the range of 10^{-4} m/s, and in some cases coincided relatively closely to the surface projected location of regional

faults. As such, conductivities measured in these wells were averaged and utilized as the conductivity for all fractures throughout the model. The remaining hydraulic conductivity measurements ranged on order from 10^{-6} m/s to $10^{-8.}$ m/s. These were applied uniformly to various layers depending on the depth of the measurement, with conductivity decreasing with depth to account for higher rock competency at depth and compression of the rock mass from the weight of overlying material (Woessner & Poeter, 2020). While deep packer test measurements were typically on order of 10^{-7} m/s, actual hydraulic conductivity at these depths was assumed to be around 10^{-8} m/s as the tests included large intervals that almost certainly intersected fractures and inflated measurements of matrix permeability. Conductivities lower than 10^{-8} m/s were not considered as they tended to cause numerical instability and excessively large hydraulic head predictions.

With consideration to groundwater flow and its representation in the hydrologic model, the geology of the local study area can be effectively simplified as large mass of hard rock (gabbroic anorthosite) where the extensive, interconnected regional fracture zones are the primary flow paths. Despite the complex rock mass of varying lithologies and tectonic alterations, all lithologic materials in the study site act as similarly impermeable matrix units interspersed with a highly conductive fault and fracture network from a hydrogeological standpoint. Though there are thin, discontinuous lenses of sedimentary material at the surface, previous studies have shown that even these tills have considerably low hydraulic conductivity that is comparable to the bedrock beneath them (Lemaire & Boyaud, 2016). However, for the purposes of parameterizing the unsaturated flow model in HGS, the top 20m layer is treated as

a uniform layer of till with respect to unsaturated hydraulic conductivities. This till layer is given a hydraulic conductivity of 10^{-6} m/s based on previous studies conducted in the region (WSP, 2016). Simplified sensitivity analysis was applied to this value, with tested variations of two orders of magnitude above and below the final value showing negligible changes in model results.

Table 2.4 - Summary of Packer Tests

Borehole	X	Y	Z (masl)	Interval	Test Model	K (m/s)
CDB-FE3-21	246767.807	5528695.838	384.82	127.3-150	Dilation	1.19E-04
CDB-FE4-21	246481.887	5529106.349	391.880	94.3-150	Dilation	7.95E-06
CDB-FE4-21	246481.887	5529106.349	391.880	121.3-150	Void Filling	1.35E-06
CDB-FE5-21	246204.864	5528801.908	382.132	73.3-150	Laminar	2.39E-04
CDB-FE5-21	246204.864	5528801.908	382.132	124.3-150	Turbulent	2.11E-06
CDB-18-03	246153.680	5528562.961	380.8374	532.3-1300	Laminar	1.26E-04
CDB-18-03	246153.680	5528562.961	380.8374	801.3-1300	Turbulent	6.84E-07
CDB-20-04	247205.170	5529470.538	380.035	792.3-1689	Turbulent	4.59E-07

2.2.4. Numerical Grid Generation

Algomesh was used to prepare the 2D model mesh for both FEFLOW and HGS (HydroAlgorithmics Pty Ltd, 2020). Based on iterative testing of the model, the final 2D mesh, optimized for computational performance and study site representation contains 46304 elements and 23387 nodes. The final 3D mesh contains 2,546,740 elements and 1,309,672 nodes (Figure 2.9). Note that in the fully coupled simulation the topography of the 3D mesh is altered vertically in the area of the lakes to represent their basins as average depths.

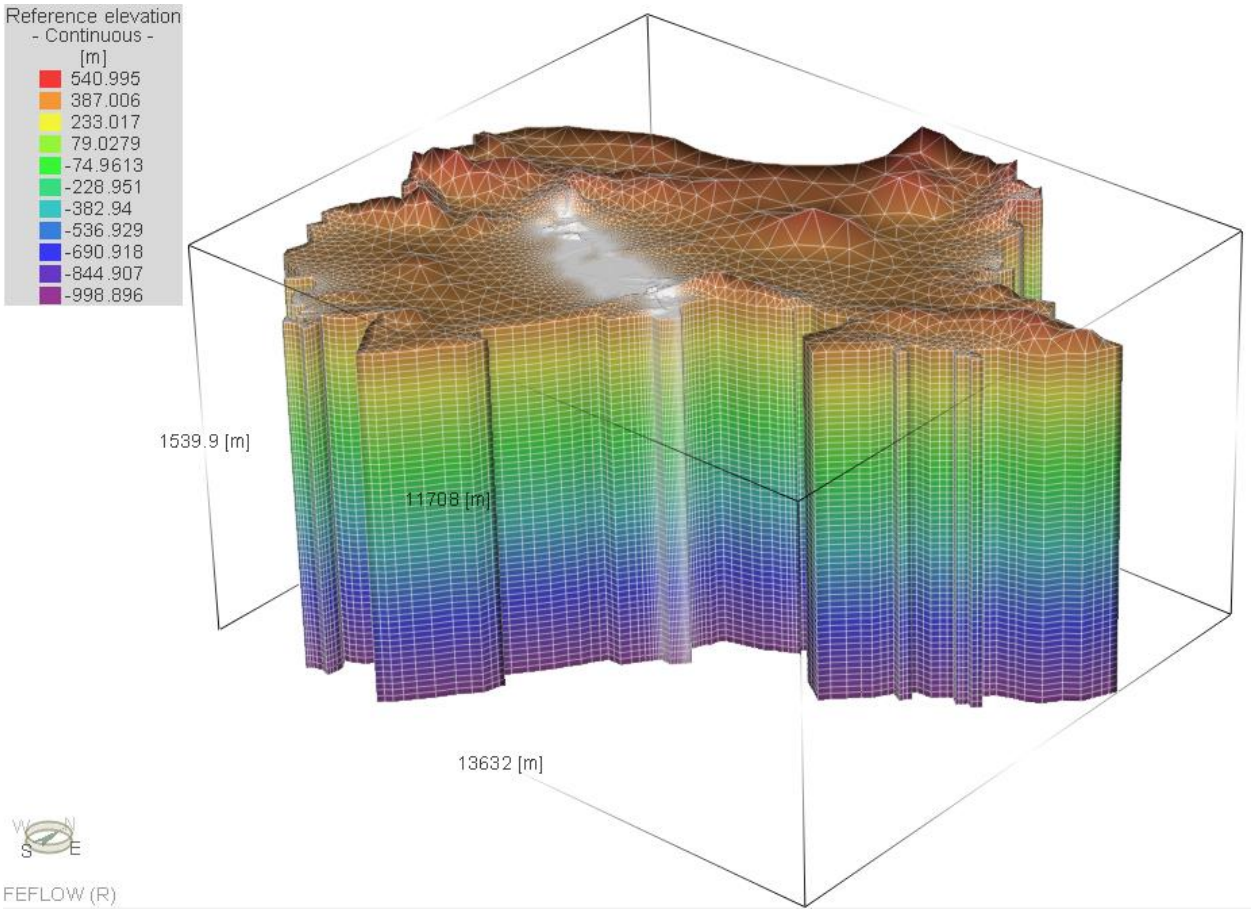


Figure 2-9 - 3D Model Mesh – FEFLOW

2.2.5. Fracture, Fault and Gallery Representation

Generalized dip angle and direction is known to be relatively steep (>70°) for some of the major fractures and shears in the model domain from historical, regional-scale measurements of these features by Daigneault & Allard (1990). For smaller fractures, it must be assumed that they will have the same dip and strike as their parent fault, which is largely inferred from the sequence of geologic events outlined in Section 2.2.2. For simplification, fractures were employed in the model as vertically dipping surface projections of their strike from the surface layer to the bottom of the model domain. Due to a lack of data on the

hydrogeologic nature of the fractures, an assumption is made that all fault and shear zones represented in the geologic map referenced are hydraulically active with an aperture equivalent to FEFLOW's default value of 1m.

Plan view surface projections of the Site A and Site B galleries were provided by Blumetric Environmental Inc (Ali Nowamooz, Personal Communication, 2021). Since the intention of the dewatering study is to determine feasibility, a conservative approach to gallery representation was taken where the surface projections are applied uniformly at depths of interest, potentially yielding a modest overestimate in dewatering volume requirements. Based on assessment of the available historical operations data and future plans outlined in Appendix VI, galleries for Site A were implemented between -398 masl and -498 masl, while Site B Galleries were implemented between -698 masl and -798 masl.

2.2.6. Sensitivity Analysis

Given the low resolution of available data, relatively large size of the study area and high complexity of the regional geology, numerous parameters remain relatively uncertain and thus challenging to calibrate. As such, sensitivity analyses were performed by varying parameters of high uncertainty in the model, conducting additional simulations and comparing rate budgets. Targets for parameter sensitivity included matrix hydraulic conductivity (each order of magnitude between 10^{-10} m/s to 10^{-5} m/s), fracture hydraulic conductivity and representation (no fractures, fractures at partial depth and fractures from top to bottom with each order of magnitude in conductivity ranging from 10^{-8} m/s to 10^{-1} m/s), and coupling length of dual nodes for fractures and land surface (10^{-6} m to 1 m).

2.2.7. Surface Parameters

No information regarding soil characteristics, evapotranspiration parameters and land topology has been directly measured in the field for this study site. As such, many of these parameters must be estimated and assumed from publicly available remote sensing data for the purposes of parameterizing the surface domain and evapotranspiration in HGS. As presented in Appendix II, observations from satellite imagery were used to divide the surface of the study site into three distinct land classes: Disturbed Land, Light Vegetation and Forest.

Rill storage in all three classes was maintained at the default HGS value of 10^{-6} m. Manning coefficients, which dictate X and Y friction for overland flow in the HGS model, were chosen for these land classes based on NLCD land classes that closely matched the description of these respective landforms, as outlined in Table 2.5 (Kalyanapu et .al, 2009).

Table 2.5 - Model Land Classes with Matching NLCD Land Classes and Associated Manning Coefficients

Model Land Classes/NLCD Associations and Resulting Manning Coefficients			
Model Land Class	NLCD Land Class - Number	NLCD Land Class - Description	Manning "n" Coefficient
Disturbed	31	Barren Land	0.0113
Light Vegetation	52	Shrub/Scrub	0.4
Forest	42	Evergreen Forest	0.32

2.3. Recharge, Climate and Evapotranspiration

The recharge of groundwater systems from meteoric and land-based sources (i.e., precipitation and infiltration from lakes and streams) is a critical component of even the most basic groundwater models. Accounting for these inputs is typically accomplished by the application of a defined flux at the surface of the model that quantifies the net rate of exchange

between the two systems Recharge may be implemented with varying degrees of discretization ranging from a constant value across the entire model (i.e., millimetres of rain per year applied to the entire surface) to discrete values in various locations on the model's surface that are transient in time.

While it is most common to incorporate a constant sitewide flux to define recharge in simpler groundwater models, this simplification tends to neglect variations in the true amount of water the groundwater system receives from the surface. For one, a constant flux derived as a yearly value ignores the wide variance in precipitation through seasonal changes during a model's runtime (Sanford, 2002). In addition, constant flux values do not account for variances in slope and soil transmissibility across a site, which are often highly heterogeneous and attenuate the true amount of water that infiltrates the ground at any given location (Sanford, 2002). Most importantly, constant recharge values cannot properly account for changes in climatic conditions that alter evapotranspiration rates throughout the year, which in turn reduce the amount of available surface water that can infiltrate an aquifer (Sanford, 2002). Even when climate factors are accounted for, they are often considered with respect to historical average values. Based on the recent development of various global climate models with multiple scenarios for future carbon emissions, it is anticipated that in nearly all cases historical average values for climate inputs will not adequately reflect real future climate parameters due to the expected changes in future climate (Intergovernmental Panel on Climate Change, 2021).

The models developed in this work utilize two different estimates of recharge. For the steady-state saturated groundwater model (and all spin-up models prior to the final fully coupled dewatering simulation), a constant recharge value is applied based on historical yearly averages of precipitation and evapotranspiration with an estimated runoff coefficient. While this represents a spatially and temporally invariant flux in the groundwater only simulations, it is important to note that fully integrated models in HGS still empirically predict runoff and soil storage. Thus, while the flux value may fixed at the surface of the model, recharge cannot be considered completely invariant as in the groundwater only simulations.

Monthly data for precipitation, maximum temperature and minimum temperature was acquired between January 1st, 1934, and January 1st, 2022 (Environment and Climate Change Canada, 2022). Average yearly precipitation was estimated from this data set at 941 mm/year. An estimated yearly evapotranspiration value was developed by applying this data to the USGS Thornthwaite Monthly Water Balance Model (McCabe and Markstrom, 2007). Thornthwaite was initially chosen as at had been used previously for similar calculations and is a proven method for estimation of evapotranspiration from a limited data set (Sentlhas et. al, 2010; Dankers, 2002). The computed yearly evapotranspiration was 457 mm/year. Runoff, which varies considerably with changes in soil and topography, was theorized based on landforms observed through satellite imagery and topographic contours from the DEM. A discrete map of runoff coefficients was generated, and the discrete values averaged to create an overall runoff coefficient for the site. The complete methodology used to determine the runoff coefficient is detailed in Appendix II. The final runoff coefficient for the site was 0.47, and the final yearly

runoff rate is given by the product of yearly precipitation and the site runoff coefficient (Equation 2.1):

Equation 2.1 – Calculation of Surface Runoff in millimetres per year

$$941\,\frac{mm}{year} \times 0.47 = 442.27\,\frac{mm}{year}\ of\ Runoff$$

Together, the balance of these components constitutes the final constant recharge value across the site as follows (Equation 2.2):

Equation 2.2 - Calculation of Historical Groundwater Recharge

$$Recharge = Precipitation - Evapotranspiration - Runoff$$

$$Recharge = 941\,\frac{mm}{year} - 457\,\frac{mm}{year} - 442.27\,\frac{mm}{year} = \mathbf{42}\,\boldsymbol{\frac{mm}{year}}$$

For the final fully coupled groundwater/surface water dewatering simulation, a transient representation of predicted future climate is applied to assess how this may influence dewatering estimates as compared to the previously derived constant recharge. The future climate data used in the model is for years 2006 – 2050 as obtained from downscaled predictions of the CMIP5 Global Climate Model Ensemble (Environment and Climate Change Canada, 2022). CMIP5 provides a robust climate model that can be acquired with statistical downscaling to the region of interest already factored into the data set when acquired from climatedata.ca (Taylor et. al, 2012). Multiple future climate prediction sets are available for CMIP5 based on variable increases in global emissions in the form of representative concentration pathway scenarios (RCP) where the primary alteration to climate is the change in

atmospheric energy flux related to natural and anthropogenic climate influences known as radiative forcing, including:

1. A best-case scenario where emissions are reduced by concerted global efforts and radiative forcing is 2.6 W/m^2 (RCP 2.6)
2. An average scenario where climate intervention does not improve beyond current efforts and emissions continue to increase on their current trajectory with radiative forcing of 4.5 W/m^2 (RCP 4.5)
3. A worst-case scenario where no intervention is undertaken, and emissions increase with radiative forcing of 8.5 W/m^2 (RCP 8.5).

For the purposes of this study, data from the RCP 8.5 scenario was used as it is assumed that the highest emission scenario will yield the most statistically significant changes in the hydrologic model with respect to dewatering volume estimates. A list of fluxes, representing the difference of CMIP5 modelled precipitation and potential evapotranspiration and discretized into 1-year intervals, was synthesized and applied to the surface of the final fully integrated dewatering model, with values ranging from 367 mm/year to 212 mm/year. Precipitation data is taken directly from the CMIP5 dataset. While HGS can calculate evapotranspiration as a rigorously derived combination of separate transpiration and evaporation processes (Aquanty, 2018), this requires extensive parameterization and significantly increases computational complexity and simulation runtime. As such, potential evapotranspiration (PET or E_p) was estimated on a monthly basis from the CMIP5 temperature data and tabulated monthly extraterrestrial solar radiation for latitude 50°N (Allen et. al, 1998)

using the Hargreaves-Samani Equation provided in Appendix II (Shahidian et. al, 2012). Runoff is not explicitly parameterized for the fully integrated model in the same way as the steady-state model, as the physically based representation of surface water flow employed by HGS utilizes the surface parameters from section 2.3.5 and the topography of the DEM to directly model this behaviour (Aquanty, 2018). The equations used by HGS to model runoff are described in Appendix I.

3. Model Results

After constructing and running the models described in the previous section, in addition to the various intermediary spin up models, results were obtained that demonstrate the predictive accuracy of each model, comparing simulated and measured hydraulic heads. It is expected that higher correlation between predicted and simulated heads is indicative of a more accurate model with respect to predicting future groundwater conditions.

Applying dewatering to both models as described in the previous section yields water balance results (also known as a rate budget) that provide volumes of water entering and leaving all components of the domain. Since the galleries are incorporated as distinct boundary conditions, the rate budgets may be used to estimate the rate of dewatering – interpreted as the steady-state rate of water leaving the galleries during the simulation – and compare the dewatering rates between each of the simulations.

The rate budget and hydraulic head results for the various FEFLOW and HGS models constructed as part of this work are presented in this section. The model scenarios capture both the natural hydrogeologic conditions at the site without dewatering and the hydrogeologic conditions induced by dewatering projected future galleries as described in Chapter 2. Model results of saturated and variably saturated results, in addition to steady state and transient simulations will be presented in order to compare how hydrogeologic conditions compare between different modeling software and different modeling scenarios.

In Section 3.1, the following base case simulations will be compared against observed data to assess their representativeness:

i) Steady State Saturated FEFLOW simulation of natural (no dewatering) conditions

ii) Steady State Saturated HGS simulation of natural (no dewatering) conditions

iii) Transient Unsaturated HGS simulation of natural (no dewatering) conditions

iv) Transient Fully Coupled Groundwater/Surface Water HGS simulation of natural (no dewatering) conditions

In Section 3.2, results will be presented for simulations where dewatering of the underground galleries are added to the base case models. Comparing these results will allow for meaningful analysis of how changes in climate/recharge and surface water integration may influence simulated results:

i) Steady State Saturated FEFLOW simulation with dewatering

ii) Steady State Saturated HGS simulation with dewatering

iii) Transient Fully Coupled Groundwater/Surface Water HGS simulation with constant historical recharge and dewatering

iv) Transient Fully Coupled Groundwater/Surface Water HGS simulation with future climate and dewatering

3.1. Base Case Simulations of Natural Conditions

Figures 3.1 and 3.2 show the hydraulic head predictions for the steady state saturated simulation for natural regional flow using FEFLOW (also referred to as the base case), as compared to the available observation data. This model was manually calibrated and achieved

a reasonable correlation between predicted and simulated hydraulic heads (R^2 = 0.59; Figure 3.1).

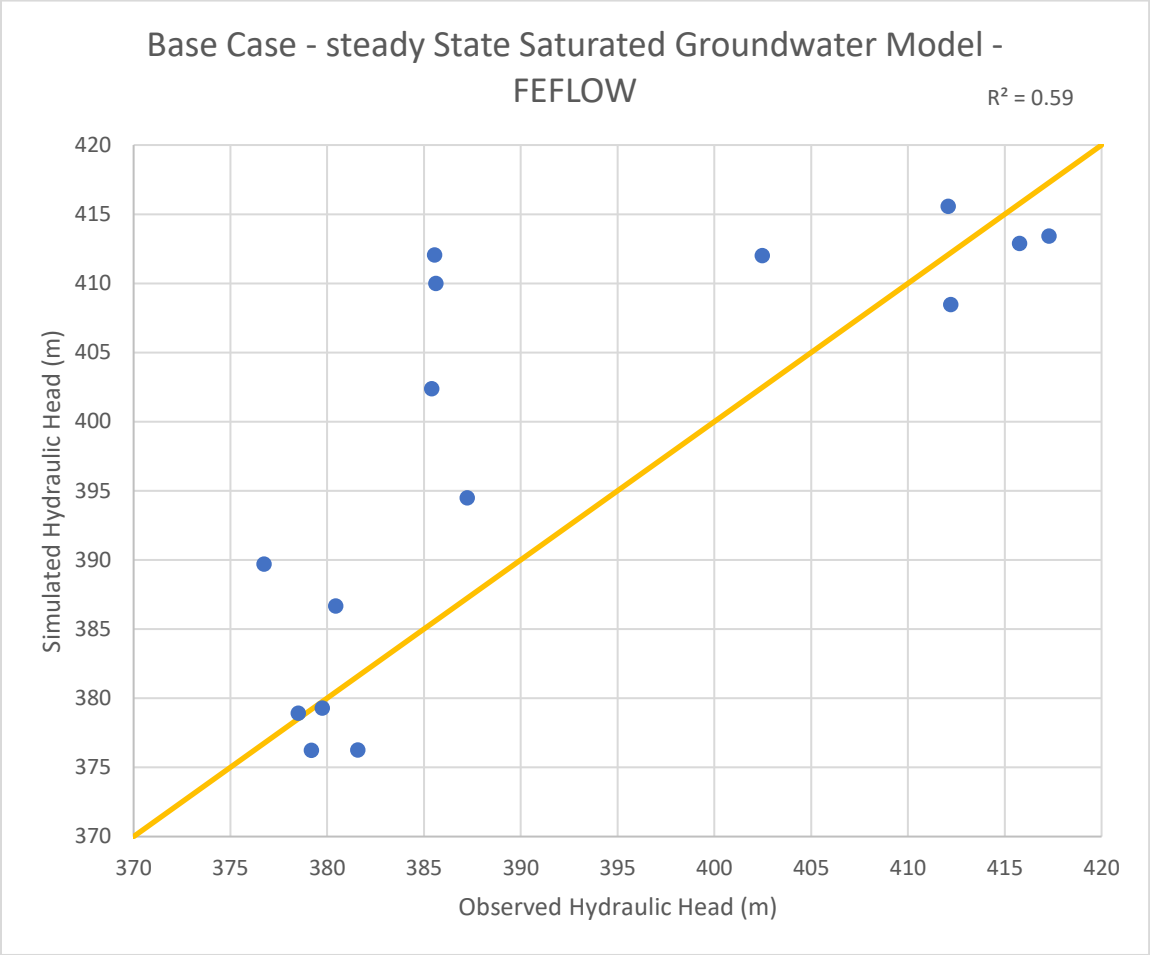


Figure 3.1 - Results of FEFLOW Base Case Simulation - Steady-State Saturated without Calibration

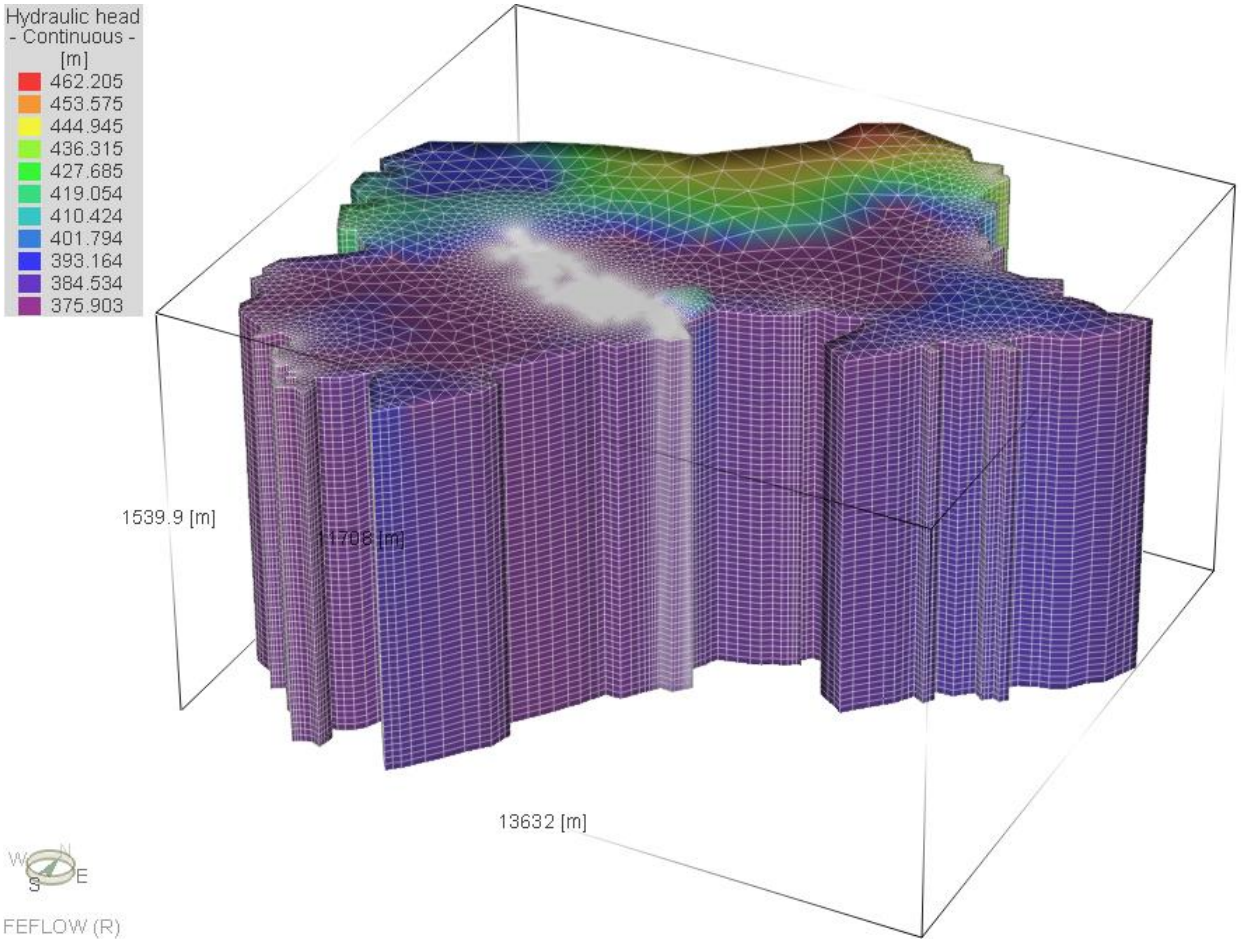


Figure 3.2 - 3D Hydraulic Head Distribution of the Steady State Saturated Base Case Model in FEFLOW

Comparatively, the results of the base case steady state simulation conducted in HGS are displayed in Figures 3.3 and 3.4. These results are generally consistent with the FEFLOW results, although they have a slightly lower R^2 value (0.57). This is likely because HGS snaps observation points to nearby nodes in the mesh, as opposed to FEFLOW which reads values from the hydraulic head isosurface. As such, the location of the observation points imported

from FEFLOW to HGS are not directly comparable. Model comparability between base case steady state conditions for FEFLOW and HGS is discussed in Appendix VII.

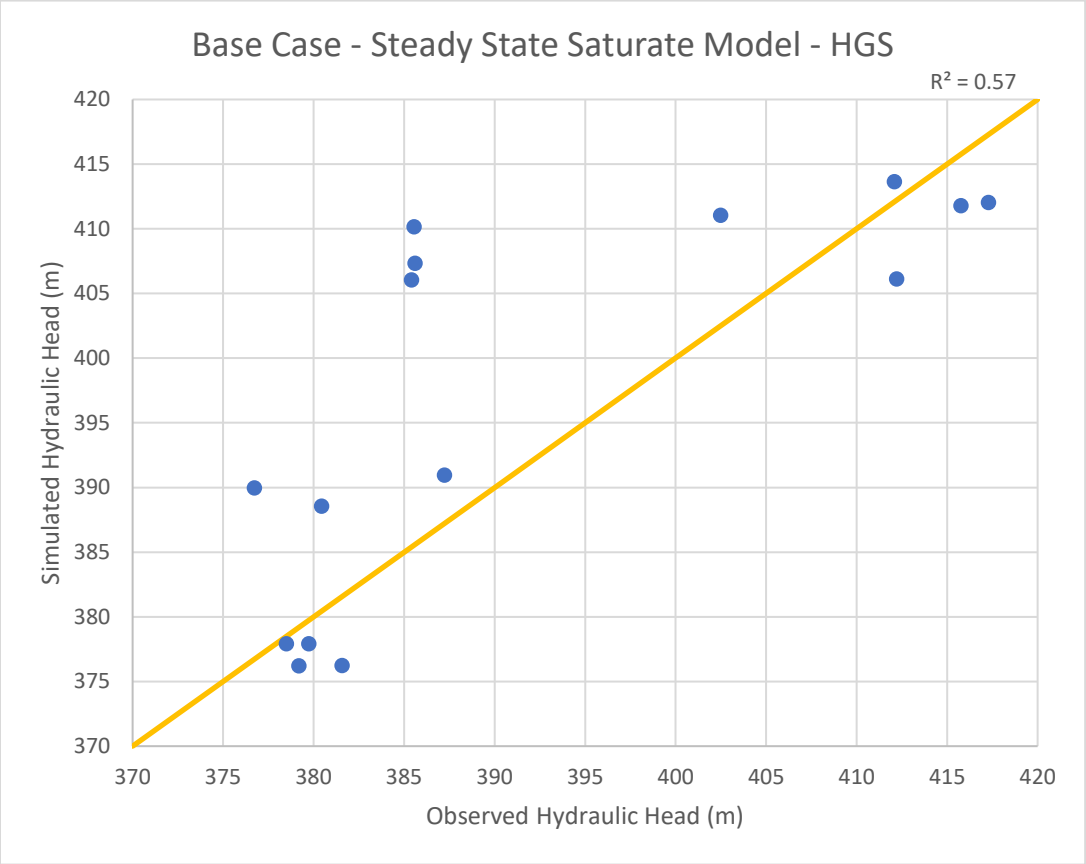


Figure 3.3 - Results of HydroGeoSphere Base Case Simulation - Steady-State Saturated

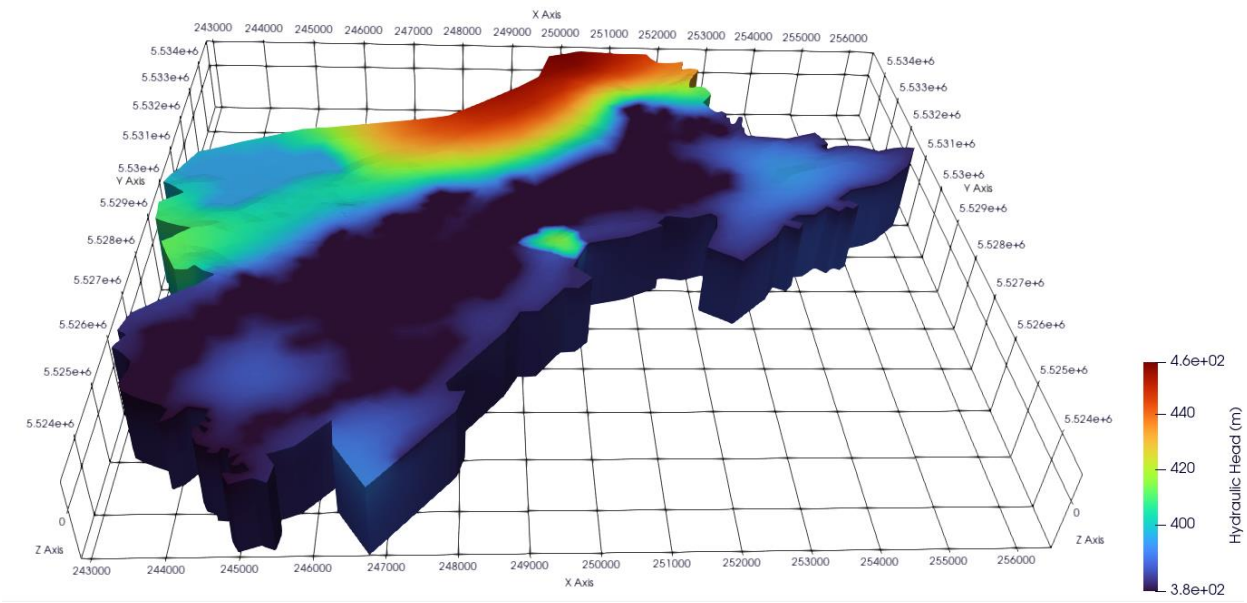


Figure 3.4 - 3D Hydraulic Head Distribution of the Steady State Saturated Base Case Model in HydroGeoSphere

Comparison of the rate budgets for the base case model in FEFLOW and HGS show that most values are generally on the same order of magnitude except for the net imbalance in each model (Table 3.1). However, given how low both imbalances are relative to total flow through the system, this is not a cause for concern.

Table 3.1 – Rate Budgets for FEFLOW and HGS Steady State Saturated Base Case Models

Base Case - Steady State Saturated Rate Budget Summary		
Model	FEFLOW	HGS
Time (Years)	N/A	N/A
Lac Dore (m^3/s)	-4.47E-02	-4.50E-02
Lac Chibougamau (m^3/s)	-9.51E-03	-9.20E-03
Lac Gilman (m^3/s)	-7.22E-03	-7.26E-03
Bottom Outflow (m^3/s)	-8.71E-06	-8.71E-06
Net Imbalance (m^3/s)	-4.67E-07	4.93E-12

The comparison of measured hydraulic heads and results from the unsaturated, transient 50-year simulation in HGS are provided in Figures 3.5 and 3.6. Though transient, this simulation is essentially run for long enough to achieve pseudo-steady state conditions (i.e., no changes to boundary conditions, and net change in the groundwater system in time is negligible after 50 years of simulation time). Addition of the unsaturated zone improves correlation between simulated and observed hydraulic heads ($R^2 = 0.62$). Note that this improvement results entirely from adding unsaturated parameters derived from standard values in Chen et. Al (2022) – no other parameters from the steady state saturated model were adjusted, and the unsaturated parameters were not optimized further.

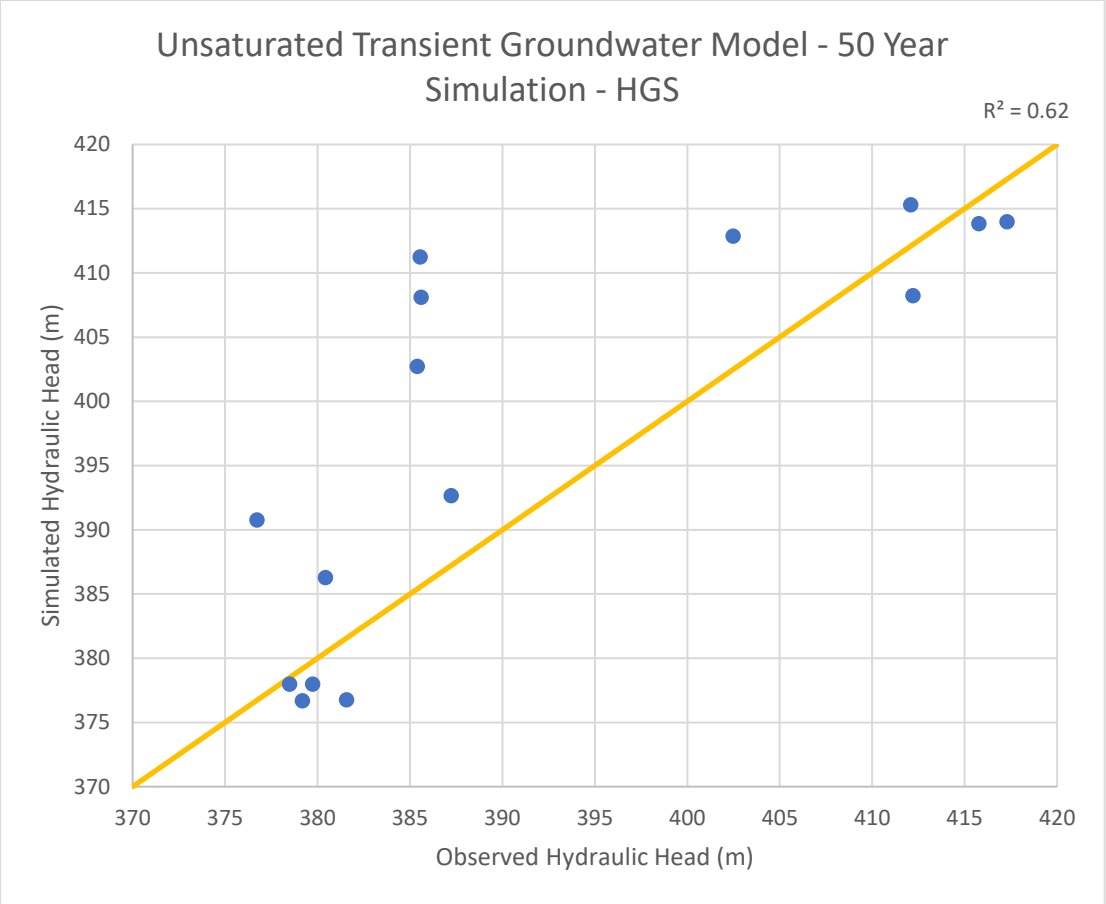


Figure 3.5 - Results of the HydroGeoSphere Base Case Simulation with Unsaturated Flow Conditions - Transient Run for 50 Years

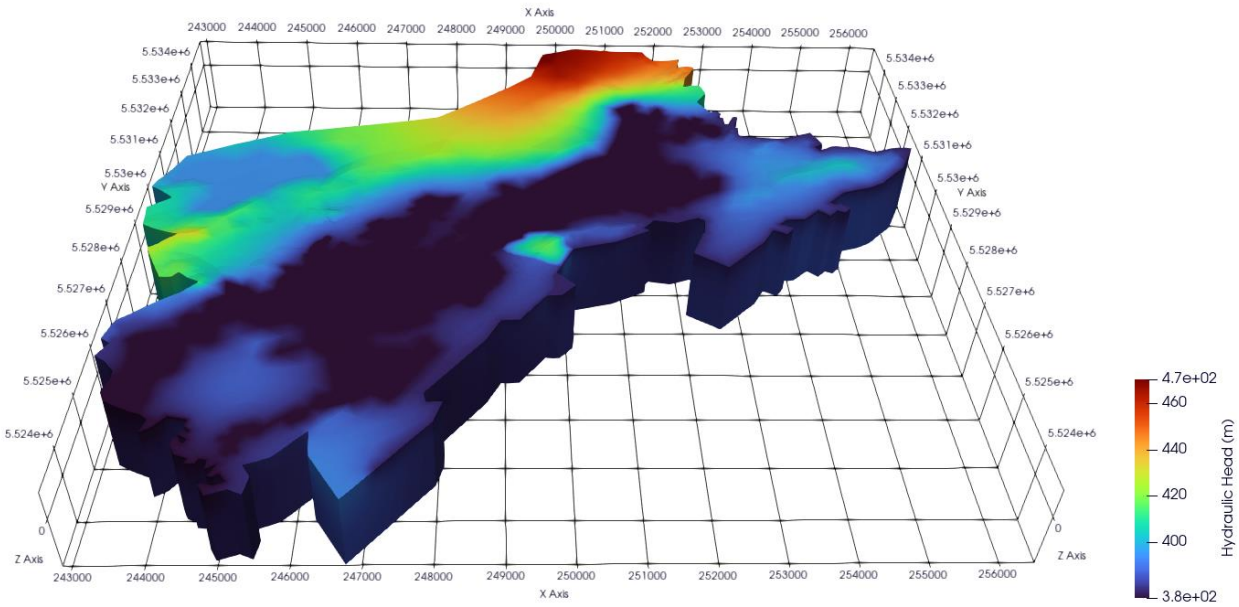


Figure 3.6 - 3D Hydraulic Head Distribution of the Transient Unsaturated Base Case Model in HydroGeoSphere

Finally, the results of the base case simulation of the study site considering unsaturated, transient groundwater flow conditions with fully coupled surface flow are presented in Figures 3.7 and 3.8. Again, the model is run for 50 years with constant boundary conditions to achieve pseudo-steady state conditions in preparation for running the final dewatering simulation. Correlation between simulated and observed hydraulic heads again improves when surface flow is coupled with the unsaturated simulation in HGS (R^2 = 0.95). This improvement results from adding standard values for surface parameters as derived from Kalyanapu et. al (2009). No additional optimization was applied to these values.

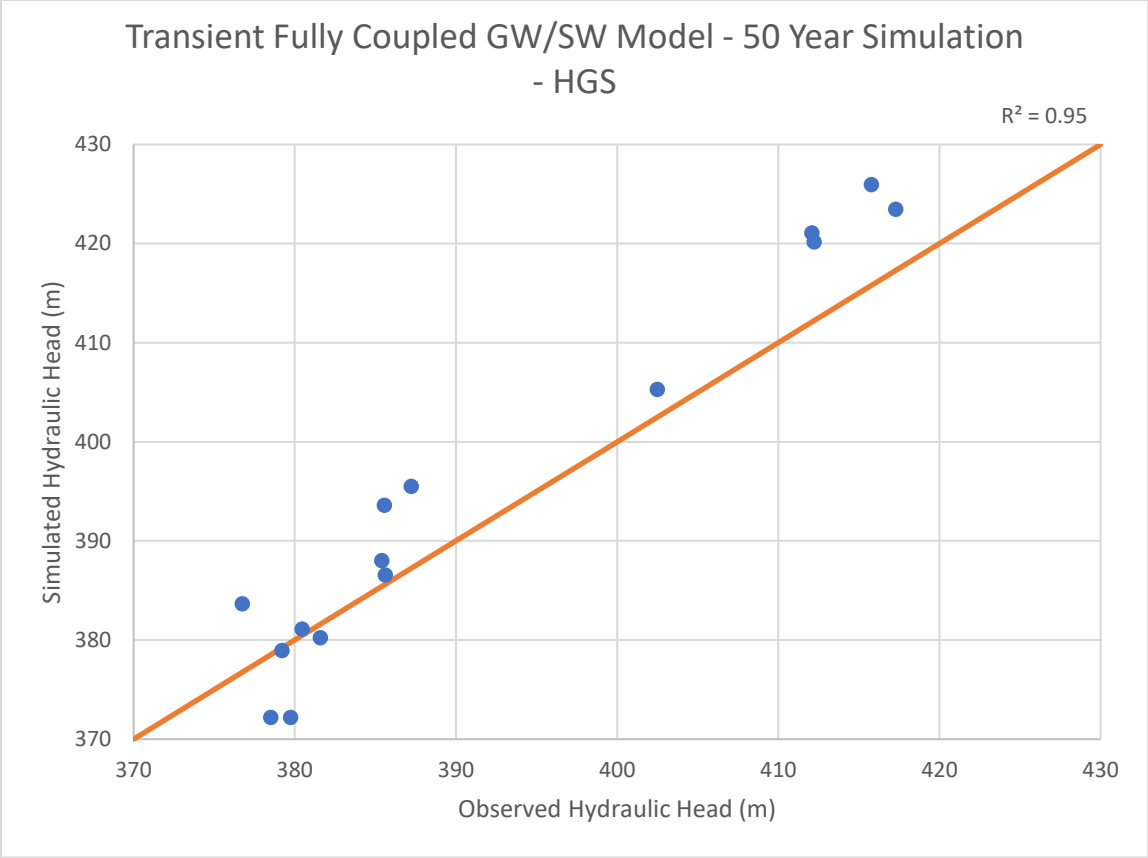


Figure 3.7 - Results of the HydroGeoSphere Fully Coupled Groundwater/Surface Water Base Case Simulation - Transient Run for 50 Years

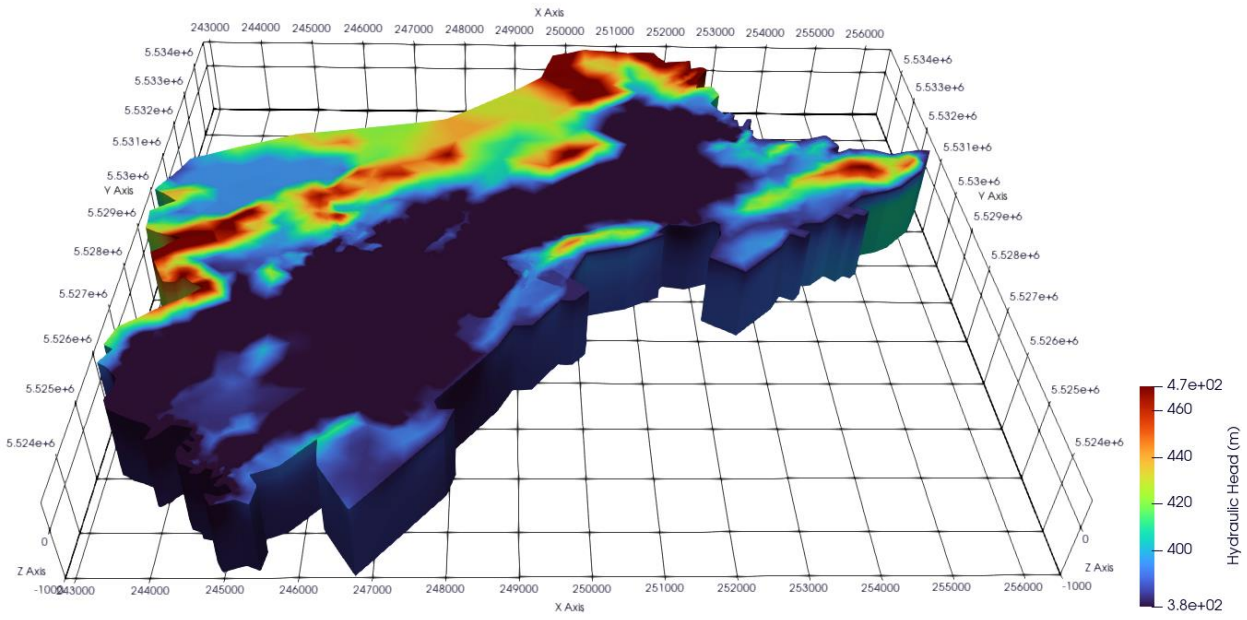


Figure 3.8 - 3D Hydraulic Head Distribution of the Fully Coupled Groundwater/Surface Water Base Case Model in HydroGeoSphere

A comparison of each calibration point to the base case model results is provided in Appendix VIII.

3.2. Simulation of Dewatering in Underground Galleries

With the base case simulation results as initial conditions, dewatering of the current and projected underground galleries will be simulated with both modeling packages. Figures 3.9 and 3.10 display the simulated drawdown due to dewatering of the steady state saturated model in FEFLOW. Note that relatively deep but confined areas of drawdown are generated directly at the shorelines where Site A and Site B are located due to the presence of Lac Dore above.

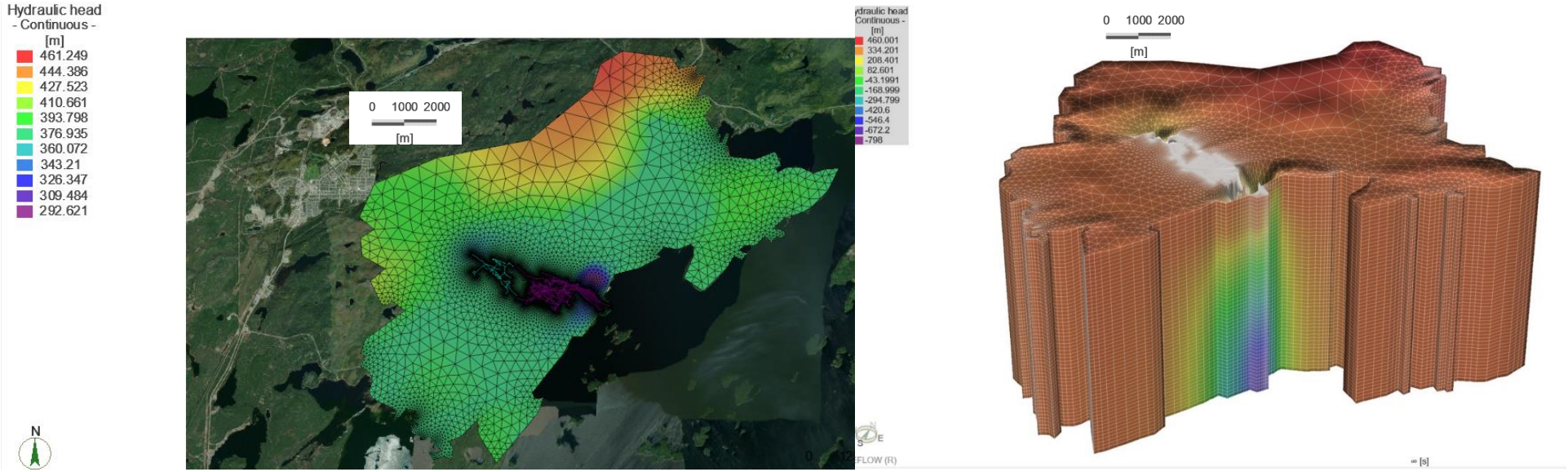


Figure 3.9 - 2D (Surface) and 3D Hydraulic Head Distribution of the Steady State Saturated Dewatering Simulation in FEFLOW

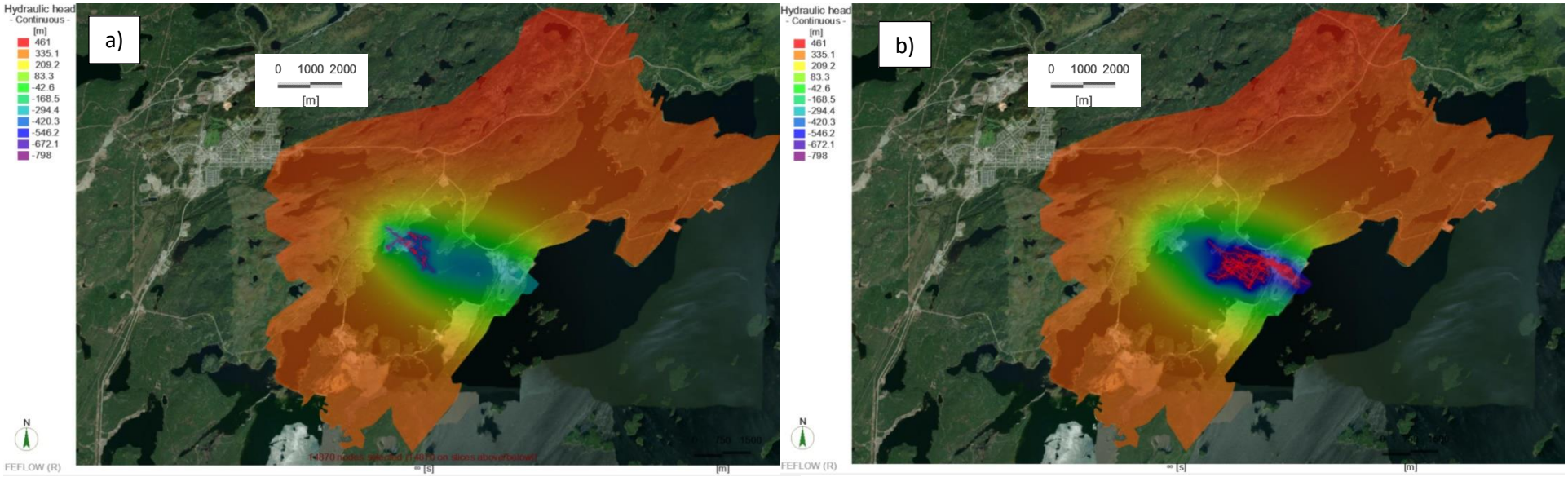


Figure 3.10 - 2D Hydraulic Head Distribution of the a) Site A and b) Site B Mine Galleries in the Steady State Saturated Dewatering Simulation in FEFLOW (Basemap modified from ESRI Satellite World Imagery)

Figure 3.11 displays the simulated drawdown due to dewatering of the steady state saturated model in HydroGeoSphere. The drawdown extent appears to be very similar between the two models despite differences in dewatering rate budget (Table 3.2). HGS does not have a free moving mesh scheme to compare changes directly with FEFLOW, but visualization of the steady-state saturated model results shows a comparable predicted zone of influence at the surface.

Table 3.2 – Summary of Water Balance Results for Dewatering Models

Dewatering Rate Budget Summary				
Model	FEFLOW - Steady State Saturated	HGS - Steady State Saturated	HGS - Fully Coupled Transient with Constant Historical Recharge - 50 Years	HGS - Fully Coupled Transient with Climate Change - 50 Years (2006 to 2056)
Time (Years)	N/A	N/A	50	50
Lac Dore (m^3/s)	3.62E-02	3.43E-02	1.79E+04	1.79E+04
Lac Chibougamau (m^3/s)	8.90E-05	8.77E-04	7.95E+00	8.01E+00
Lac Gilman (m^3/s)	-3.26E-03	-2.27E-03	2.93E+03	2.93E+03
Bottom Outflow (m^3/s)	6.92E-06	8.71E-06	8.73E-06	8.73E-06
Surface Outflow (m^3/s)	N/A	N/A	-2.09E+04	-2.09E+04
Site A Galleries (m^3/s)	-3.35E-02	-3.28E-02	-3.39E-02	-3.38E-02
Site B Galleries (m^3/s)	-6.26E-02	-6.16E-02	-6.30E-02	-6.27E-02
Net Imbalance	-1.67E-03	-1.61E-12	-3.35E-04	1.25E-02

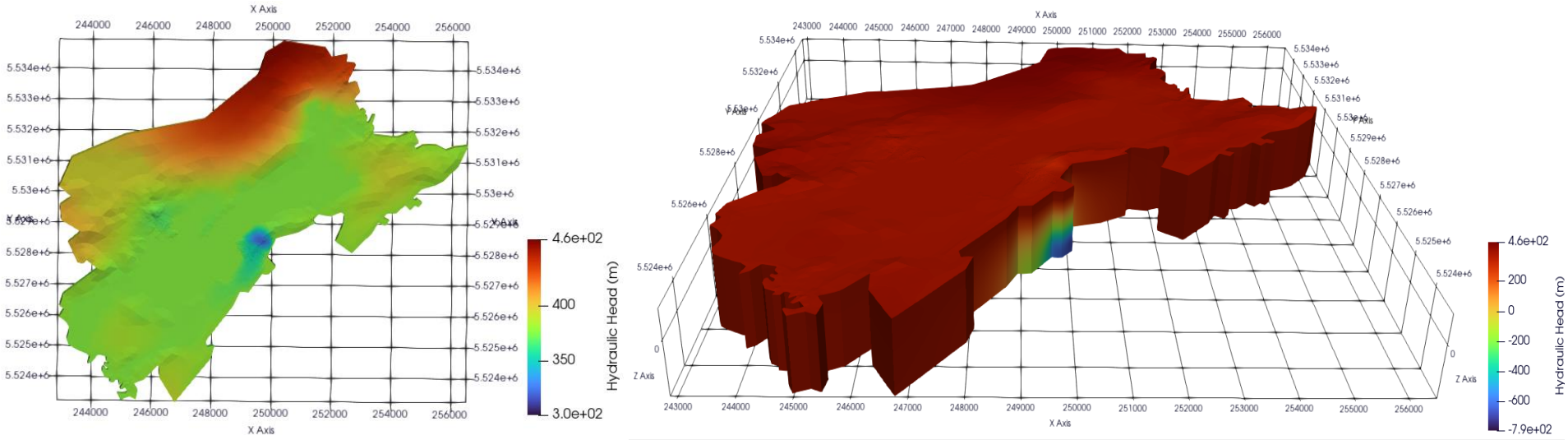


Figure 3.11 - 2D (Surface) and 3D Hydraulic Head Distribution of the Steady State Saturated Dewatering Simulation in HydroGeoSphere

Figure 3.12 displays the simulated drawdown due to dewatering for the fully coupled groundwater/surface water model in HGS applying a constant recharge based on historical climate averages as in all previous models.

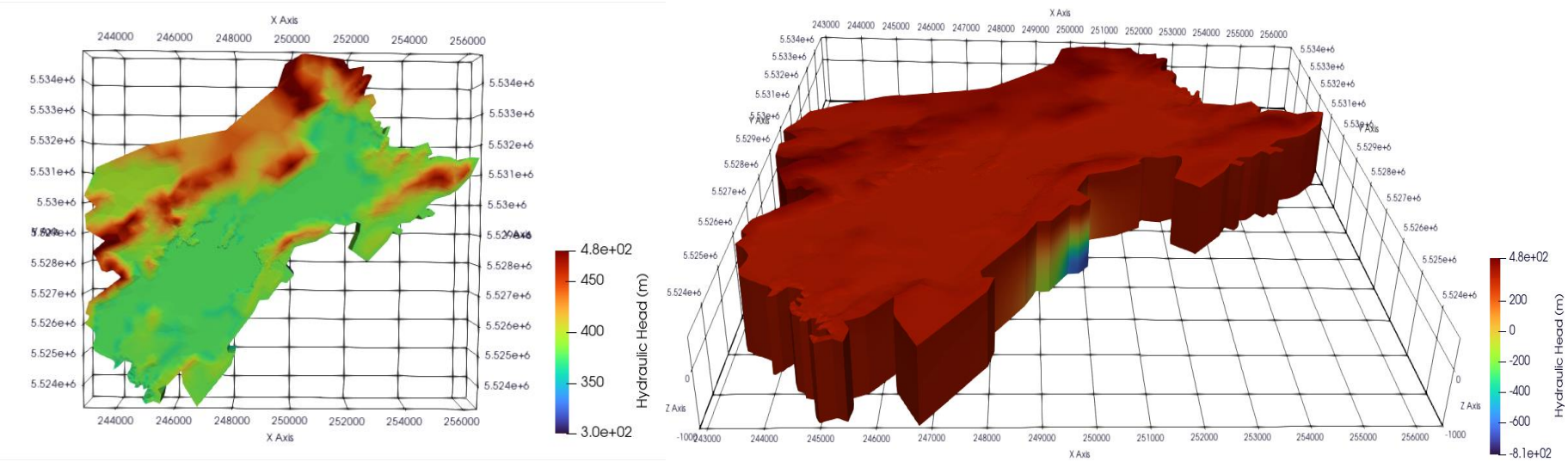


Figure 3.12 - 2D (Surface) and 3D Hydraulic Head Distribution of the Fully Coupled Groundwater/Surface Water Dewatering Simulation with Historical Climate Forcing in HydroGeoSphere

Finally, Figure 3.13 displays the simulated drawdown due to dewatering for the fully coupled groundwater/surface water model in HGS when temporal changes in total precipitation and evapotranspiration from the future global climate model are applied as climate forcing.

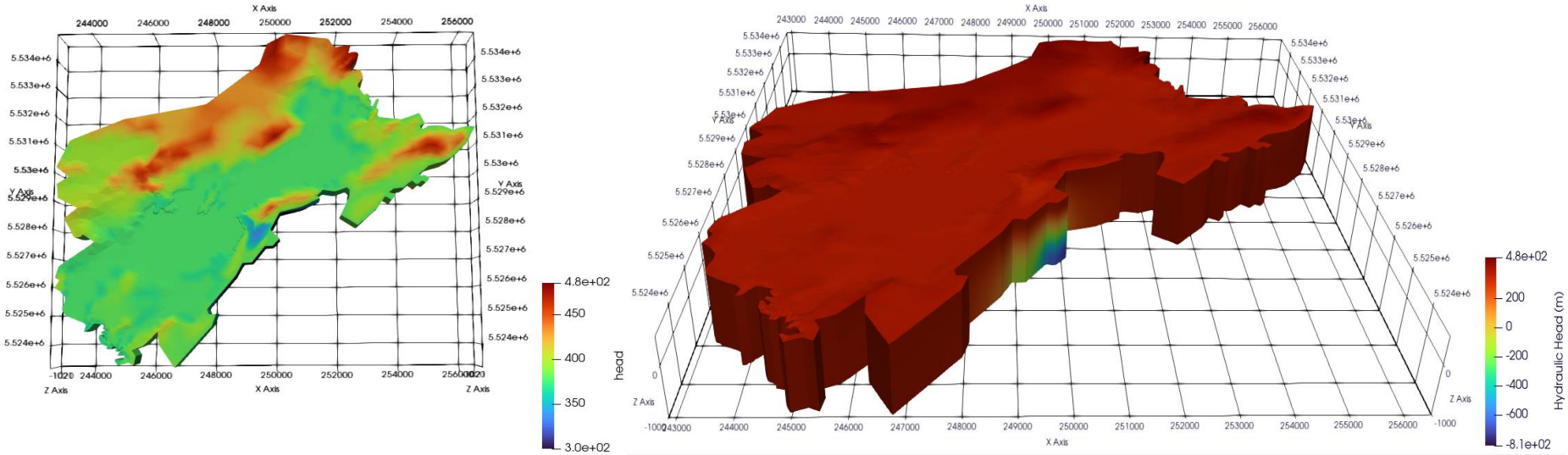


Figure 3.13 - 2D (Surface) and 3D Hydraulic Head Distribution of the Fully Coupled Groundwater/Surface Water Dewatering Simulation with Future Climate Forcing in HydroGeoSphere

Rate budgets serve numerous analytical purposes in this study; to assess overall changes to the groundwater system, to compare the relatability of similar models built in HGS and FEFLOW, and to infer required pumping rates for the underground mining galleries. The dewatering rate from the galleries can be inferred from the rate of water leaving the seepage boundary conditions that define them. When converted to more commonly used m^3/day in pumping applications, these results demonstrate that there is an increase in predicted dewatering rate of approximately 32 m^3/day, or 0.38%, between the steady state groundwater dewatering model using FEFLOW and the transient fully coupled hydrologic dewatering model with climate forcing in HGS (Table 3.3). When comparing to the steady saturated model in HGS, the predicted increase in dewatering rate with climate and surface water coupling increases to approximately 182 m^3/day, or 2.22% (Table 3.3).

Table 3.3 - Summary of Dewatering Rates

Summary of Dewatering Rates (m^3/day)				
Model Case	FEFLOW - Steady State Saturated	HGS - Steady State Saturated	HGS - Fully Coupled Transient - Historical Climate	HGS - Fully Coupled Transient - Future Climate
Site A Galleries	-2891.64	-2831.55	-2932.95	-2919.84
Site B Galleries	-5411.66	-5322.44	-5442.30	-5415.83
Total	-8303.30	-8153.99	-8375.25	-8335.67
Difference Between FEFLOW Steady State and HGS Fully Coupled:			-71.95	-32.37
Difference Between HGS Steady State and HGS Fully Coupled:			-221.26	-181.68

4. Discussion

Predicted fluxes for each boundary condition in the base case steady-state saturated models are relatively similar between HGS and FEFLOW (Table 3.1). Outflow rates from the constant head boundaries defining Lac Dore, Lac Chibougamau, and Lac Gilman are on the same order of magnitude (10^{-2} m^3/s, 10^{-3} m^3/s, and 10^{-3} m^3/s respectively), and vary by as much as 2.71% between FEFLOW and HGS simulations. The only notable discrepancies between the HGS and FEFLOW results is in the mass balance error, which is significantly lower in HGS (on the order of 10^{-12}) than FEFLOW (on the order of 10^{-7}), though both are a sufficiently small percentage of total flow to imply accurate solution by each matrix solver (approximately 7.6 x 10^{-4} % of total flow in FEFLOW and 8.02 x 10^{-9} % of total flow in HGS).

Visual inspection of the resulting surface shows qualitatively that the results of the HGS model are very similar to those of the FEFLOW model. Any minor differences can likely be attributed to the differences in numerical implementation between the two programs. As Quantitatively, the models can be compared through synthetic pilot points that are centred on mesh nodes, allowing for equivalent representation in FEFLOW and HGS as demonstrated by the high R^2 value of 0.99 (Figures 4.1 and 4.2).

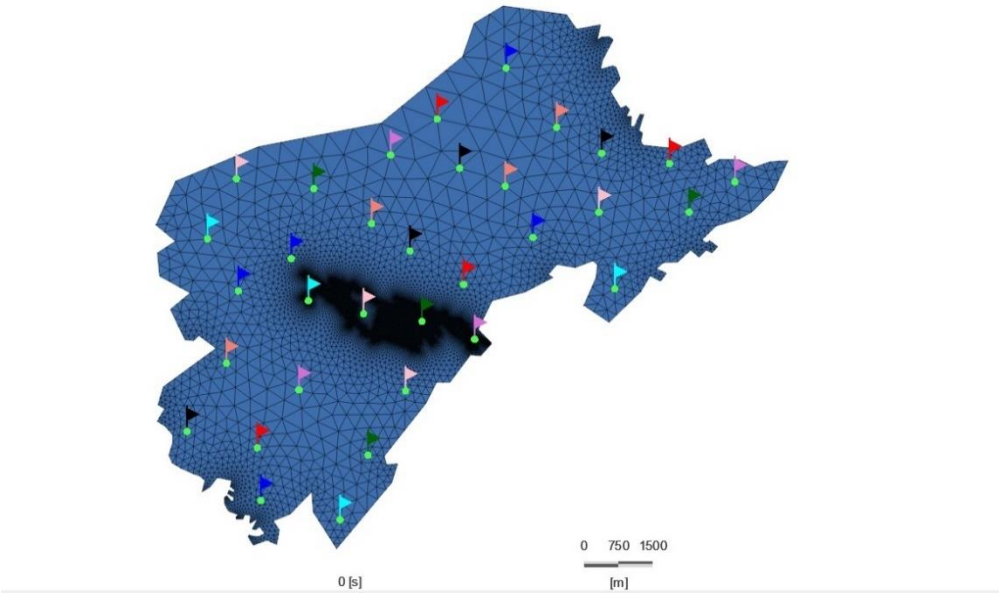


Figure 4.1 - Locations of Synthetic Pilot Points

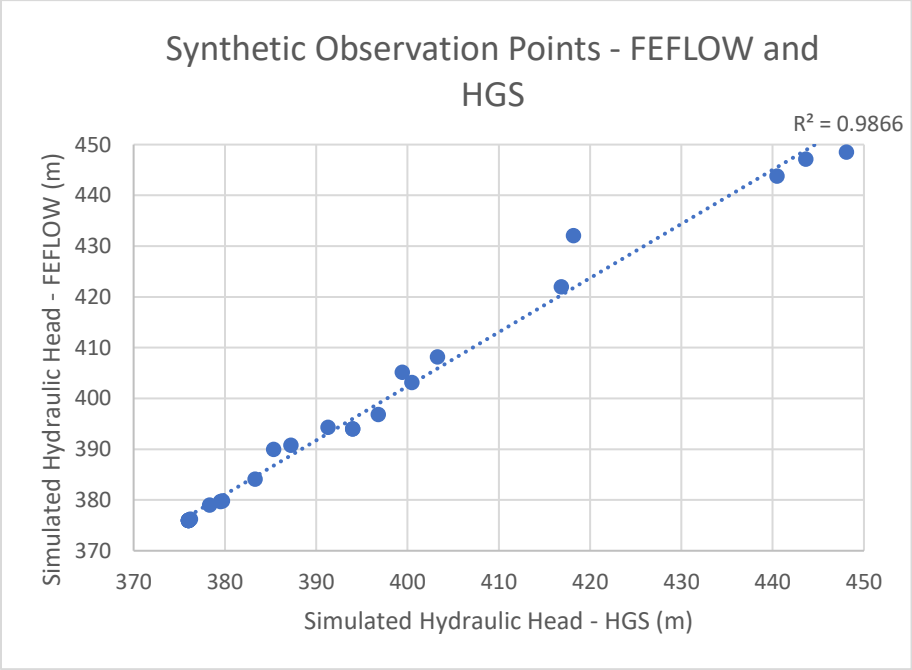


Figure 4.2 - Hydraulic Head Correlation Between Synthetic Pilot Points in FEFLOW and HydroGeoSphere

The summary of predicted dewatering rates in Table 3.3 indicates that the fully coupled HGS model with future climate forcing predicts greater dewatering rates than either steady state dewatering model based on historic climate, with the disparity being greater between the steady state HGS model and the fully coupled HGS model. However, for the downscaled 50-year dataset of CMIP5 climate predictions used at this site, the temporal trend in overall changes to precipitation and evapotranspiration shows a decrease in meteoric water input with time (Figure 4.1). In essence, dewatering rates are greater in the fully-integrated simulations despite decreasing input from precipitation, likely due to the large additional fluid input to the galleries from more directly connecting surface water sources to the subsurface. This increases immediate fluid availability to the galleries that may exceed typical recharge rates in the groundwater only model, and thus necessitate greater dewatering rates to maintain empty galleries. From examining the change in surface water boundary fluxes in Table 3.2, one can reasonably infer that simply adding surface water coupling to the model yields much more withdrawal (averaging approximately 6.35×10^7 % more withdrawal from all lake boundaries in the fully coupled HGS model as compared to the steady state FEFLOW model) from the boundaries defining the surface water system. This is likely due to a significant increase in immediate fluid availability from the lakes to the galleries which, as previously noted, are directly connected at the surface. It is also notable that FEFLOW employs a free moving mesh scheme for its top layer to represent movement of the water table, whereas HGS does not. This may result in resizing of elements in the top layer and alter near surface storage in the simulation, which could account not only for differences between the steady state saturated groundwater model in FEFLOW and HGS, but also differences between steady state

groundwater dewatering simulation in FEFLOW and fully coupled transient dewatering simulation in HGS.

Similarly, flow rates from the boundaries are drastically increased between the groundwater only and fully integrated model – increasing on an order between 10^4 m^3/day and 10^6 m^3/day from the former to the latter. With large reservoirs of water directly connected to the galleries, dewatering rates form the fully integrated model may overcome any potential limitations in recharge between the surface and the subsurface seen in the groundwater only model due pumping rates exceeding fluid availability from soil storage and recharge from the surface. Further, it is possible that HGS predicts greater soil storage in the fully integrated models, thereby providing more fluid to be removed from the galleries. Similarly, solver differences between FEFLOW (Picard iteration with Algebraic Multigrid) and HGS (Newton iteration) are likely accountable for differences in rate budgets and results.

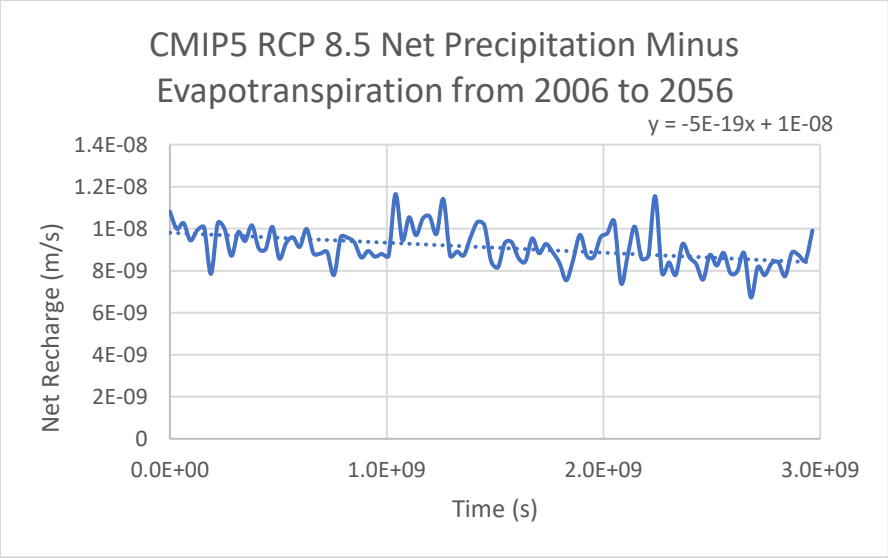


Figure 4.3 - Trend in Net Recharge Over Time Applied as Climate Forcing for the Fully Coupled Transient HGS Dewatering Model

4.1. Uncertainty

Based on limited sensitivity analysis conducted during model construction, the greatest source of uncertainty in this model is the parameters that define the fracture network (Appendix IX). Employing a dual node scheme for fracture flow results in a predicted dewatering rate that is approximately 30% of what is predicted by a common node scheme. In FEFLOW, the choice of dual node or common node fracture implementation yields a tenfold difference in dewatering rates (i.e. rates increase from being on the order of 10^3 m^3/day to 10^4 m^3/day) when switching from dual node to common node, shown in Appendix IX. Generally, the common node approach in which hydraulic head is represented as a continuum between the surface and subsurface is considered the most physically sensible representation of domain coupling (De Rooij, 2017). However, previous studies have shown that sufficiently accurate and physically representative results can be readily obtained with a dual node scheme of sufficiently small coupling length while also allowing for drastically more efficient computation and greater stability in complex problem domains (De Rooij, 2017). Dual node implementation was chosen as the rates yielded were far more physically sensible, and to maintain comparability between models as the fully coupled HGS model was unable to converge when employing common node fracture scheme.

The changes in rates yielded by common node and dual node schemes of varying coupling lengths are illustrated in the Dual Node Connector Documentation of the FEFLOW Help Documentation (DHI Group, 2022). In general, increasing the coupling length between matrix and fractures reduces their connectivity, forcing more of the flow in the system to occur

in the fracture network with less interaction or dispersion into the matrix (Figure 4.4). Changes to coupling length under a dual-node scheme had significant impacts on predicted rates, with rates increasing as coupling length is reduced (i.e. moving closer to common node equivalency). Coupling length was maintained in the models at 10^{-2} m, which has been demonstrated as an ideal coupling length in prior literature (Ebel et. al, 2009). This also proved to be the smallest coupling length for which the fully coupled model was able to achieve convergence (Liggett et. al, 2012). Finally, changes in coupling conductivity had significant impacts on hydraulic head predictions and rate budget. However, no good metric could be determined for parameterizing this value, and the value cannot be changed in FEFLOW. In both FEFLOW and HGS, default coupling hydraulic conductivity for dual node fractures is 0 m^3/s, which represents no advective exchange and only diffusive exchange between fractures and the matrix. This value was used across all models and appears to be most physically sensible as the conceptual model assumes that groundwater flow in the domain is primarily through the fracture network. This assumption is based on inferences from the geologic model of the site, where the gabbroic anorthosite that makes up the entire subsurface is assumed to have negligible primary porosity, deriving its total porosity almost entirely from fracturing and shearing.

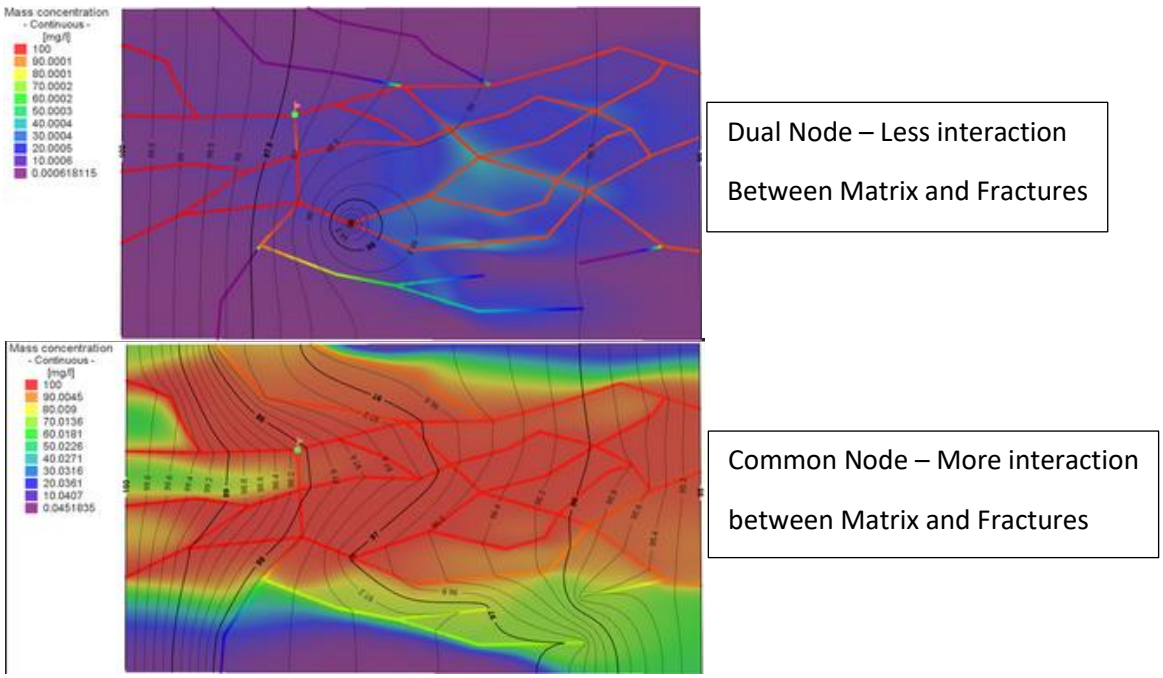


Figure 4.4 - Differences in Fracture/Matrix Interaction Between Dual Node and Common Node Scheme (Modified from DHI Group, 2022)

Very little is known about the fractures at the study site beyond their surface projections. While dip and strike are known for the main regional shear zones, the many branching fractures have not been directly measured. It can be assumed that fractures of the same strike likely result from the same orogeny and thus have similar dips, but this would need verification. Ultimately, the fractures were simplified with vertical dips that would maintain their interaction with the underground galleries and yield conservatively high dewatering estimates. However, its possible that incorporating their true inclination could change the overall groundwater flow scheme in the model.

Fracture aperture was maintained at FEFLOW's default value of 1 metre across all models and assumed to have no clogging material. Informal discussions with individuals affiliated with the site owners indicate that this is not an unreasonable assumption for the main

shear zones across the site, but ultimately there is no quantitative measure of this metric for the broader fracture network. While this estimate is unrealistically large for the entire network of fractures, it provides a conservative overestimate of dewatering rate which will provide more applicable for real world water management design applications at the site. In addition, limited sensitivity testing demonstrated that varying the fracture aperture from 0.01 metre to 1 metre showed negligible change in water budgets through the galleries (0.01% difference), suggesting that reducing the aperture to a more realistic average would have minimal influence on the results.

Previous studies show that discontinuities in fractured flow paths are far more common than the continuous flow path of uniform aperture assumed here, as fracture apertures begin to close at greater depths and sediment transport within fractures can induce clogging (Viswanathan et. al, 2021). In addition, hydraulic conductivity for the fractures was based on the highest values yielded in packer testing near known fracture locations but, given the large packer intervals utilized in testing, likely represents a much lower value than reality. Still, sensitivity testing demonstrated that changes to fracture aperture and conductivity appeared to have minimal impact on predicted hydraulic heads and dewatering rates relative to coupling parameters for dual nodes.

Typically, physically based surface flow in HGS would require full representation of the basin for each water body in the model domain. This was infeasible for this model given the sheer size of the lakes in the model relative to the area of interest and the available time and computing power for simulations. As such, Lac Dore was incorporated as a partial basin while

Lac Chibougamau was simply maintained as a Southern Boundary in the model. However, this implementation made it extremely difficult to properly replicate expected lake levels in the model. As such, constant head boundary conditions were maintained over the entirety of the lakes in the final fully integrated model. While this ensures proper lake levels, it also prevents changes to the lake levels in response to changes in the overall surface water flow regime. This would almost certainly influence predicted dewatering rates as flow from the lakes to the fracture network driven by surface water levels and storage would be fixed.

Finally, many of the parameters used to prepare the fully integrated model are derived from average material values sourced from literature review rather than direct field measurements, including Van Genuchten parameters for the unsaturated zone and Manning Coefficients for the surface. While all values are reasonable for the expected materials and hydraulic head predictions were excellent when adding these parameters, direct field measurements of these values could likely improve model predictability.

4.1.1. Uncertainties in Observational Data

Observational data used in the construction and calibration of the groundwater model was interpreted within the bounds of numerous challenges and limitations with respect to data quality and quantity at the study site. While inconsistencies in the observational values do not impact the results and conclusions of this study, they are important to consider in the context of real-world representativeness for the study site itself.

The resolution of available calibration data is rather poor given the large extent of the study site. There are only 15 available hydraulic head measurements for calibration of a model

with an area spanning nearly 100 km^2 which, realistically, could be much larger still if all lake basins were properly implemented in the fully coupled groundwater/surface water model. At the very least, these measurement points are close to the sites of interest and ensure accurate predictability directly in the area of the galleries, but there is no reliable way to ascertain that predicted heads around the outer limits of the model are accurate beyond ensuring that they do not exceed the land surface. However, the artesian conditions observed in Site B further increase this uncertainty as artesian conditions in other areas of the domain cannot be ruled out.

While inaccurate hydraulic heads in the outer limits of the model may not directly affect predictions within the area of the galleries, they would certainly affect groundwater storage/supply in the model and flow between the groundwater system and surface water bodies over the study site. Anomalously high hydraulic heads in areas of high topographic relief near Site B required manual calibration with a lower hydraulic conductivity zone, equivalent to the lowest hydraulic conductivity value at depth extended to the surface of the model in this location. Additional field measurements of hydraulic conductivity in the wells throughout this zone would greatly improve model calibration.

In addition, the available observation points vary in their date of collection, possibly representing drastically different site conditions at the time of measurement. Further, it is known that many of the wells used to measure the observational data are steeply dipping, but the exact nature of dip and dip direction was not available at the time of data preparation. In

the future, this additional information may be accounted for, and may necessitate additional calibration of the groundwater model.

5. Conclusions and Recommendations

To determine how fully integrated watershed modelling and climate change may influence predictions made by dewatering simulations, a robust conceptual model was developed and implemented in both FEFLOW and HGS to assess changes in model rate budgets with varying model parameters and components. After conceptualizing the study site and constructing numerical models to simulate base case and dewatering conditions for steady state saturated groundwater and transient fully integrated groundwater/surface water representations of the area, simulation results showed that the addition of surface water coupling and climate forcing based on future climate models yielded a maximum estimate of approximately 188 m^3/day more dewatering for underground mining galleries at the study site than the comparable steady state saturated groundwater only model, representing an increase of approximately 2%.

Further, this study also demonstrates that physically based surface water coupling has the potential to improve predictive accuracy of traditional groundwater models, as the fully coupled model results increased fit metrics from as low as $R^2 = 0.57$ in the saturated model to $R^2 = 0.95$ in the fully coupled run. Finally, modelling results showed that, with careful accounting of all parameters, a groundwater model in FEFLOW may be replicated in HGS.

The fully coupled hydrologic model was used to simulate a future climate scenario, using CMIP RCP 8.5 forcings. These results indicate that even when P-ET is decreasing with time, a fully coupled groundwater/surface water model of the study site will predict greater dewatering requirements than a comparable groundwater only model for this site. It would be

valuable to explore the relationship between surface water coupling, climate and dewatering rates for underground and open pit mines without such uniquely direct connections to large fracture networks as those observed in this study. Furthermore, this study only utilized maximum emission scenarios from the CMIP5 global climate model, but numerous alternative cases exist within the same model data set. As such, it would be valuable to explore similar fully coupled simulations with additional climate scenarios to assess the sensitivity of model predictions to variations in predicted global climate changes.

Finally, numerous limitations in data quality and quantity are acknowledged in the parameterization and calibration of this model and it is likely that further data collection and analysis may reveal a need for recalibration of the groundwater model to better represent real world site conditions.

References

Allen, R. G., Pereira, L. S., Raes, D., & Smith, M. (1998). Annex 2. Meteorological Tables. *Crop evapotranspiration - Guidelines for computing crop water requirements.* Food and Agricultural Organization of the United States. https://www.fao.org/3/X0490E/x0490e0j.htm#annex%202.%20meteorological%20tables

Appiah-Adjei, E. K. (2006). Climate Change Impacts on Groundwater Recharge in Gulf Islands, Canada (thesis).

Aquanty. (2018). *HydroGeoSphere Theory Manual*. Waterloo, ON, Canada.

Beck, H. E., Zimmermann, N. E., McVicar, T. R., Vergopolan, N., Berg, A., & Wood, E. F. (2018). Present and future Köppen-Geiger climate classification maps at 1-km resolution. *Scientific Data*, *5*(1). https://doi.org/10.1038/sdata.2018.214

Blodgett, S., & Kuipers, J.R. (2002). Subsidence and hydrologic environmental Impacts. Technical Report on underground hard-rock mining, Center for Science in Public Participation, pp 36–38

Brunner, P., & Simmons, C. T. (2011). Hydrogeosphere: A fully integrated, physically based Hydrological Model. *Ground Water, 50*(2), 170–176. https://doi.org/10.1111/j.1745-6584.2011.00882.x

Cahyadi, T. A., Magdalena, S., Haryanto, D., Ratminah, W. D., Rosadi, P. E., & Asmara, P. E. (2020). Planning of Mining Water Management Costs. *2nd International Conference on Earth Science, Mineral, and Energy*. https://doi.org/10.1063/5.0007076

Chen, J., Sudicky, E. A., Davison, J. H., Frey, S. K., Park, Y.-J., Hwang, H.T., Erler, A. R., Berg, S. J., Callaghan, M. V., Miller, K., Ross, M., & Peltier, W. R. (2019). Towards a climate-driven simulation of coupled surface-subsurface hydrology at the Continental Scale: A Canadian example. *Canadian Water Resources Journal / Revue Canadienne Des Ressources Hydriques, 45*(1), 11–27. https://doi.org/10.1080/07011784.2019.1671235

Chen, Y.F., Ye, Y., Hu, R., Yang, Z., & Zhou, C.B. (2022). Modeling unsaturated flow in fractured rocks with scaling relationships between hydraulic parameters. *Journal of Rock Mechanics and Geotechnical Engineering, 14*(6), 1697–1709. https://doi.org/10.1016/j.jrmge.2022.02.008

Cochand, F., Therrien, R., & Lemieux, J.-M. (2018). Integrated Hydrological Modeling of climate change impacts in a snow-influenced catchment. *Groundwater, 57*(1), 3–20. https://doi.org/10.1111/gwat.12848

Daigneault, R., & Allard, G. (1990) *MM 89-03. Le Complexe du Lac Doré et son environnement géologique (Région de Chibougamau - sous-province de l'Abitibi).* Government du Quebec.

Dankers, R. (2002). *Sub-arctic hydrology and climate change a case study of the Tana River basin in northern Fennoscandia* (dissertation). Koninklijk Nederlands Aardrijkskundig Genootschap, Utrecht.

De Rooij, R. (2017). New insights into the differences between the dual node approach and the common node approach for coupling surface–subsurface flow. *Hydrology and Earth System Sciences, 21*(11), 5709–5724. https://doi.org/10.5194/hess-21-5709-2017

DHI Group. (2022). *FEFLOW 7.5 Documentation*. FEFLOW 7.5 Documentation. Retrieved April 12, 2022, from http://www.feflow.info/html/help75/feflow/

Diersch Hans-Jörg, G. (2016). *Feflow: Finite element modeling of flow, mass and heat transport in porous and fractured media*. Springer.

Dong, D., Lin, G., Lin, Y.-F. F., Zhao, M., & Li, K. (2014). Evaluating induced fractures between a large artificial lake and an aquifer-coal seam system: A case study in tangshan coal mine, China. *Mine Water and the Environment, 35*(2), 253–260. https://doi.org/10.1007/s10230-014-0319-z

Dong, D., Sun, W., & Xi, S. (2012). Optimization of mine drainage capacity using FEFLOW for the no. 14 coal seam of China's linnancang coal mine. *Mine Water and the Environment, 31*(4), 353–360. https://doi.org/10.1007/s10230-012-0205-5

Earman, S., & Dettinger, M. (2011). Potential impacts of climate change on Groundwater Resources – A Global Review. *Journal of Water and Climate Change*, 2(4), 213–229. https://doi.org/10.2166/wcc.2011.034

Ebel, B. A., Mirus, B. B., Heppner, C. S., VanderKwaak, J. E., & Loague, K. (2009). First-order exchange coefficient coupling for simulating surface water-groundwater interactions: Parameter sensitivity and consistency with a physics-based approach. *Hydrological Processes, 23*(13), 1949–1959. https://doi.org/10.1002/hyp.7279

Environment and Climate Change Canada and ClimateData.ca. (2022). *Historical Daily Total Precipitation - Chibougamau, QC*. https://climatedata.ca/download/

Evans, L. (2019). (tech.). *REDACTED Property Summary*. REDACTED. Retrieved October 25, 2022, from https://www.REDACTED.com/wp-content/uploads/2021/05/RPA_REDACTED_NI43-101-Report-FINAL_June_15_2019.pdf.

Freeze, R. A., & Harlan, R. L. (1969). Blueprint for a physically-based, digitally-simulated hydrologic response model. *Journal of Hydrology, 9*(3), 237–258. https://doi.org/10.1016/0022-1694(69)90020-1

Freeze, R. A., & Witherspoon, P. A. (1966). Theoretical analysis of regional groundwater flow: 1. analytical and numerical solutions to the mathematical model. *Water Resources Research, 2*(4), 641–656. https://doi.org/10.1029/wr002i004p00641

Goderniaux, P., Brouyère, S., Fowler, H. J., Blenkinsop, S., Therrien, R., Orban, P., & Dassargues, A. (2009). Large scale surface–subsurface hydrological model to assess climate change impacts on groundwater reserves. *Journal of Hydrology, 373*(1–2), 122–138. https://doi.org/10.1016/j.jhydrol.2009.04.017

GPS Nautical Charts. (2022, May 21). Lac Aux Dores Boating App #11.19/49.8318/-74.3565. i-Boating: Free Marine Navigation Charts and Fishing Maps. https://fishing-app.gpsnauticalcharts.com/i-boating-fishing-web-app/fishing-marine-charts-navigation.html?title=Dores+Lac+Aux+boating+app#11.19/49.8329/-74.3583

Hashemi, H., Uvo, C. B., & Berndtsson, R. (2015). Coupled modeling approach to assess climate change impacts on groundwater recharge and adaptation in arid areas. *Hydrology and Earth System Sciences, 19*(10), 4165–4181. https://doi.org/10.5194/hess-19-4165-2015

Hu, L., Zhang, M., Yang, Z., Fan, Y., Li, J., Wang, H., & Lubale, C. (2020). Estimating dewatering in an underground mine by using a 3D finite element model. *PLOS ONE, 15*(10). https://doi.org/10.1371/journal.pone.0239682

HydroAlgorithmics Pty Ltd. (2020). *Algomesh 2 User Guide.* Retrieved November 4, 2022, from https://dl.hydroalgorithmics.com/AlgoMesh%20User%20Guide.pdf

Intergovernmental Panel on Climate Change. (2021, August 9*). Climate change widespread, rapid, and intensifying*. IPCC. https://www.ipcc.ch/2021/08/09/ar6-wg1-20210809-pr/

Jenkin, G. R., Lusty, P. A., McDonald, I., Smith, M. P., Boyce, A. J., & Wilkinson, J. J. (2014). Ore deposits in an evolving Earth: An introduction. *Geological Society, London, Special Publications*, 393(1), 1–8. https://doi.org/10.1144/sp393.14

Kalyanapu, A. J., Burian, S. J., & McPherson, T. N. (2009). Effect of land use-based surface roughness on hydrologic model output. *Journal of Spatial Hydrology, 9*(2). https://scholarsarchive.byu.edu/josh/vol9/iss2/2

Karssenberg, D., Schmitz, O., Salamon, P., de Jong, K., and Bierkens, M. F. P. (2009). A software framework for construction of process-based stochastic spatio-temporal models and data assimilation, Environmental Modelling & Software 25(4), 489-502, 2010. doi: 10.1016/j.envsoft.2009.10.004.

Kollet, S.J. & Maxwell, R.M. (2006). Integrated surface-groundwater flow modeling: a free-surface overland flow boundary condition in a parallel groundwater flow model. *Advances in Water Resources, 29(7), 945-958,* doi:10.1016/j.advwatres.2005.08.006.

Langevin, C.D., Hughes, J.D., Banta, E.R., Provost, A.M., Niswonger, R.G., & Panday, S. (2017). MODFLOW 6 Modular Hydrologic Model: U.S. Geological Survey Software, https://doi.org/10.5066/F76Q1VQV

Leclerc, F., Roy, P., Houle, P., Pilote, P., Bédard, J. H., Harris, L. B., McNicoll, V. J., Breeman, O. van, David, J., & Goulet, N. (2017). (rep.). *RG2015-03. Géologie de la région de Chibougamau*. Government du Quebec.

Lemaire, D., & Boyaud, C. (2016). *Modélisation Hydrogéologique Project de Restauration Mine Principale Chibougamau (Québec)*. WSP Canada Inc.

Liggett, J. E., Werner, A. D., & Simmons, C. T. (2012). Influence of the first-order exchange coefficient on simulation of coupled surface–subsurface flow. *Journal of Hydrology, 414–415*, 503–515. https://doi.org/10.1016/j.jhydrol.2011.11.028

Lou, S., Liu, S., Ma, G., Zhong, G., & Li, B. (2018). Fully integrated modeling of Surface Water and groundwater in coastal areas. *Journal of Hydrodynamics, 30*(3), 441–452. https://doi.org/10.1007/s42241-018-0047-0

Martineau, G. (1984). *Géologie du Quaternaire de la Région de Chibougamau*. Bibliothèque nationale du Québec.

McCabe, G. J., & Markstrom, S. L. (2007). A monthly water-balance model driven by a graphical user interface. *Open-File Report*. https://doi.org/10.3133/ofr20071088

Ministère des Forêts, de la Faune et des Parcs. (2019). *LiDAR (pleine résolution) - 32G9xx and 32G16xx. Forêt ouverte*. Gouvernement du Québec. https://www.foretouverte.gouv.qc.ca/

Mousavi, A., & Sellers, E. (2019). Optimisation of production planning for an innovative hybrid underground mining method. *Resources Policy, 62,* 184–192. https://doi.org/10.1016/j.resourpol.2019.03.002

Mu, W., Wu, Q., Xing, Y., Qian, C., Wang, Y., & Du, Y. (2018). Using numerical simulation for the prediction of mine dewatering from a karst water system underlying the coal seam in the Yuxian Basin, Northern China. *Environmental Earth Sciences, 77*(5). https://doi.org/10.1007/s12665-018-7389-3

Prairie Climate Centre. (2019). Climate Atlas of Canada, version 2 (July 10, 2019). https://climateatlas.ca

QGIS.org. (2022). *QGIS Geographic Information System*. QGIS Association. http://www.qgis.org

RadonEx Ltd. (2011). *REDACTED Project Summary.* REDACTED. May 2011.

Rapantova, N., Grmela, A., Vojtek, D., Halir, J., & Michalek, B. (2007). Ground water flow modelling applications in mining hydrogeology. *Mine Water and the Environment*, *26*(4), 264–270. https://doi.org/10.1007/s10230-007-0017-1

Sanford, W. (2002). Recharge and groundwater models: An overview. *Hydrogeology Journal, 10*(1), 110–120. https://doi.org/10.1007/s10040-001-0173-5

Scibek, J., & Allen, D. M. (2006). Modeled impacts of predicted climate change on recharge and groundwater levels. *Water Resources Research, 42*(11). https://doi.org/10.1029/2005wr004742

Sentelhas, P. C., Gillespie, T. J., & Santos, E. A. (2010). Evaluation of FAO penman–monteith and alternative methods for estimating reference evapotranspiration with missing data in Southern Ontario, Canada. *Agricultural Water Management*, *97*(5), 635–644. https://doi.org/10.1016/j.agwat.2009.12.001

Shahidian, S., Serralheiro, R., Serrano, J., Teixeira, J., Haie, N., & Santos, F. (2012). Hargreaves and other reduced-set methods for calculating evapotranspiration. *Evapotranspiration - Remote Sensing and Modeling.* https://doi.org/10.5772/18059

Statistics Canada. 2023. (table). Census Profile. 2021 Census of Population. Statistics Canada Catalogue no. 98-316-X2021001. Ottawa. Released March 29, 2023. https://www12.statcan.gc.ca/census-recensement/2021/dp-pd/prof/index.cfm?Lang=E (accessed June 19, 2023).

Szczepiński, J. (2019). The significance of Groundwater Flow Modeling Study for simulation of opencast mine dewatering, flooding, and the Environmental Impact. *Water, 11*(4), 848. https://doi.org/10.3390/w11040848

Taylor, K. E., Stouffer, R. J., & Meehl, G. A. (2012). An overview of CMIP5 and the experiment design. *Bulletin of the American Meteorological Society, 93*(4), 485–498. https://doi.org/10.1175/bams-d-11-00094.1

Thomason, C. (2019). Chapter 4 - Hydrology, Section 12 - Rational Method. In *Hydraulic Design Manual*. Texas Department of Transportation.

Van der Kwast, H. (2021). Derive all subcatchments from a DEM using PCRaster in QGIS. YouTube. Retrieved April 12, 2022, from https://www.youtube.com/watch?v=5uGaLIlaFh8.

Van Roosmalen, L., Sonnenborg, T. O., & Jensen, K. H. (2009). Impact of climate and land use change on the hydrology of a large-scale agricultural catchment. Water Resources Research, 45(7). https://doi.org/10.1029/2007wr006760

Viswanathan, H. S., Ajo-Franklin, J. B., Birkholzer, J. T., Carey, J. W., Guglielmi, Y., Hyman, J. D., Karra, S., Pyrak-Nolte, L., Rajaram, H., Srinivasan, G., & Tartakovsky, D. M. (2021*). From Fluid Flow to Coupled Processes in Fractured Rock: Recent Advances and New Frontiers.* https://doi.org/10.1002/essoar.10508014.1

Waterloo Hydrogeologic. (2016). *Aquifertest 11.0 Help*. Retrieved April 12, 2022, from https://www.waterloohydrogeologic.com/help/aquifertest/

Winter, T. C. (1978). Numerical simulation of steady state three-dimensional groundwater flow near Lakes. *Water Resources Research, 14*(2), 245–254. https://doi.org/10.1029/wr014i002p00245

Woessner, W. W., & Poeter, E. P. (2020). Conditions Effecting Hydraulic Conductivity Values. In *Hydrogeologic Properties of Earth Materials and Principles of Groundwater Flow*. essay, The Groundwater Project.

WSP. (2016). *Modélisation hydrogéologique. Restauration du site Mine Principale.* Rapport produit pour

Yang, X., Hu, J., Ma, R., & Sun, Z. (2021). Integrated hydrologic modelling of groundwater-surface water interactions in cold regions. *Frontiers in Earth Science, 9.* https://doi.org/10.3389/feart.2021.721009

Appendices

Appendix A: HydroGeoSphere Governing Equations

HydroGeoSphere simultaneously simulates flow in the surface and subsurface by intrinsically coupling the diffusion wave approximation of the 2D surface flow equation (Equation A.1) with momentum (Equation A.2) and a modified form of Richard's equation for variably saturated groundwater flow (Equation A.3). The equations are coupled via an exchange flux term (Aquanty, 2018).

Equation 0.1 - 2D Diffusive Wave Equation

$$2D\ Diffusive\ Wave\ Equation: -\nabla \cdot d_0 q_0 - d_0 \Gamma_0 \pm Q_0 = \frac{\partial \phi_0 h_0}{\partial t}$$

Where:

d_0 = Depth of Flow (L)

q_0 = Fluid Flux (L t^{-1})

$d_0\Gamma_0$ = Volumetric Fluid Exchange Rate (L t^{-1})

Q_0 = Volumetric Flowrate for External Sources/Sinks (L t^{-1})

ϕ_0 = Surface Flow Domain Porosity (dimensionless)

h_0 = Water Surface Elevation (L)

Equation 0.2 - Coupling Momentum with the 2D Saint Venant Equation

$$\frac{\partial}{\partial t}(\bar{v}_{xo}d_o) + \frac{\partial}{\partial x}(\bar{v}^2{}_{xo}d_o) + \frac{\partial}{\partial y}(\bar{v}_{xo}\bar{v}_{yo}d_o) + gd_o\frac{\partial d_o}{\partial x} = gd_o(S_{ox} - S_{fx})$$

$$\frac{\partial}{\partial t}(\bar{v}_{yo}d_o) + \frac{\partial}{\partial y}(\bar{v}^2{}_{yo}d_o) + \frac{\partial}{\partial x}(\bar{v}_{xo}\bar{v}_{yo}d_o) + gd_o\frac{\partial d_o}{\partial y} = gd_o(S_{oy} - S_{fy})$$

Where:

$\bar{v}_{xo}$ and $\bar{v}_{yo}$ = Vertically average flow velocities in the X and Y direction (L/t)

g = Acceleration Due to Gravity on Earth (L/t^2)

S_{fx} and S_{fy} = Friction Slopes in the X and Y Direction (Dimensionless)

S_{ox} and S_{oy} = Bed Slopes in the X and Y Direction (Dimensionless)

Equation 0.3 - Richard's Equation

$$Richard's\ Equation: -\nabla \cdot (\omega_m q) + \sum \Gamma_{ex} \pm Q = \omega_m \frac{\partial}{\partial t}(\theta_s S_w)$$

Where:

ω_m = Volumetric fraction of total matrix porosity (dimensionless)

q = Fluid Flux ($L\ t^{-1}$)

Γ_{ex} = Volumetric Fluid Exchange Rate ($L^3\ L^{-3}\ t^{-1}$)

Note that Γ_{ex} may apply to more than just exchange to this surface water domain (i.e. wells, fractures, tile drains). The sum of all exchange terms Γ_{ex} is represented as a total exchange flux

Γ_0 which is necessary for coupling the governing equations. When Γ_0 is positive, this conventionally represents flow into the porous medium from the other domains.

θ_s = Saturated Volumetric Water Content (dimensionless)

S_w = Water Saturation (dimensionless)

Q = Fluid Exchange to Outside of Simulation Domain ($L^3\ L^{-3}\ t^{-1}$)

t = Time (t)

Equations for the two flow domains are coupled either by a pressure head at a common node, or via a dual node approach where flow between the two mediums is coupled via the Volumetric Fluid Exchange Rate Γ_0 with some prescribed separation distance between nodes in the two domains known as the coupling length (Aquanty, 2018; Equation A.4). The use of two nodes assumes the existence of some porous exchange medium partitioning the surface and subsurface domains with a thickness equivalent to the coupling length. The dual node approach is generally more robust. The equation for the exchange flux term Γ_0 in the dual node approach is given by (Aquanty, 2018):

Equation 0.4 - Dual Node Exchange Flux

$$\Gamma_0 = \frac{\omega_m k_r K_{zz}}{l}(h - h_0) + \frac{\omega_d k_{dr} K_{dzz}}{l}(h_d - h_0)$$

Where:

k_r = Relative Permeability of the Subsurface (dimensionless)

k_{dr} = Relative Permeability of the Dual Medium (dimensionless)

K_{zz} = Subsurface Vertical Saturated Hydraulic Conductivity (L/t)

K_{dzz} = Dual Medium/Exchange Vertical Saturated Hydraulic Conductivity (L/t)

l = Node Coupling Length (L)

h = Subsurface Hydraulic Head (L)

h_0 = Surface Water Hydraulic Head (L)

h_d = Dual Medium/Exchange Hydraulic Head (L)

Surface runoff in HydroGeoSphere is physically based and determined by calculation of the dimensionless bed and friction slopes in the X and Y direction (Equation A.5). For this study, the Manning equation was used for this calculation, though HydroGeoSphere also allows for Chezy or Darcy-Weisbach Equations.

Equation 0.5 - Manning Equation

$$S_{fx} = \frac{\bar{v}_{xo}\bar{v}_{so}n_x^2}{d_o^{4/3}}$$

$$S_{fy} = \frac{\bar{v}_{yo}\bar{v}_{so}n_y^2}{d_o^{4/3}}$$

Where:

$\bar{v}_{so}$ = Vertically Avraged Velocity Along the Direction of Maximum Slope (L/t)

n_x and n_y = Manning Roughness Coefficients in the X and Y Directions (Dimensionless)

Appendix B: Recharge Equations

Historical total precipitation rate was determined by taking the average of yearly total precipitation in millimetres between 1934 and 2022. Evapotranspiration was determined by the average of all yearly totals for actual evapotranspiration predicted by the USGS Thornthwaite Monthly Water Balance Model (McCabe & Markstrom, 2007).

For estimating actual evapotranspiration (AET), Thornthwaite first calculates potential evapotranspiration (PET) as a function of monthly daylight hours (determined by latitude) and mean monthly temperature using the Hamon Equation (McCabe & Markstrom, 2007; Equation A.6):

Equation 0.6 - Potential Evapotranspiration

$$PET = 13.97 \times d \times D^2 \times \left(\frac{4.95 \times e^{0.062T}}{100}\right)$$

Where:

d = Number of days in a month

D = Mean monthly hours of daylight in units of 12 hours

T = Mean Monthly Temperature (°C)

When total precipitation for the month is less than PET, then AET is equal to the sum of total precipitation and the available soil moisture for withdrawal, with soil moisture withdrawal rate deceasing linearly with soil moisture storage as the soil dries. When the sum of total precipitation and soil moisture storage withdrawal is less than PET, than a soil moisture deficit

is recorded as PET-AET (McCabe & Markstrom, 2007). If total precipitation exceeds PET, AET equals PET and any excess moisture replenishes soil moisture storage. When soil moisture storage exceeds capacity, water becomes available for runoff.

Runoff volume is calculated as a percentage of total precipitation using a runoff coefficient (C) that is dependent on the characteristics of the land surface (Equation A.7). Runoff (Ro) is influenced by the slope of the land surface (C_t), vegetation in the area (C_v) and the local soil conditions (C_s) (WSP, 2016; Equation A.8).

Equation 0.7 - Runoff Volume

$$Ro = P \cdot C$$

Equation 0.8 - Runoff Coefficient

$$C = C_t + C_v + C_s$$

Where:

C = Runoff Coefficient (dimensionless)

C_t = Slope Factor Coefficient (dimensionless)

C_v = Vegetation Factor Coefficient (Dimensionless)

C_s = Soil Factor Coefficient (Dimensionless)

Runoff is a challenging parameter to assign for the study area due to the drastic changes in slope and topography and high heterogeneity of surface landforms (Figure A.1). Furthermore, a large portion of the study area has not been directly observed or studied with respect to surficial properties or runoff characteristics, and thus could only be inferred by

approximations from satellite imagery. For the slope factor, calculations of slope percentage were made within each pixel on the elevation DEM (Figure A.2) for the site using the GDAL slope tool in QGIS (QGIS.org, 2022), and then the resulting DEM was refactored such that slope percentages were categorized into respective slope factor coefficients (Figure A.3), based on info available from the Texas Department of Transportation's Hydraulic Design Manual and represented in a new DEM (Thomason, 2019).

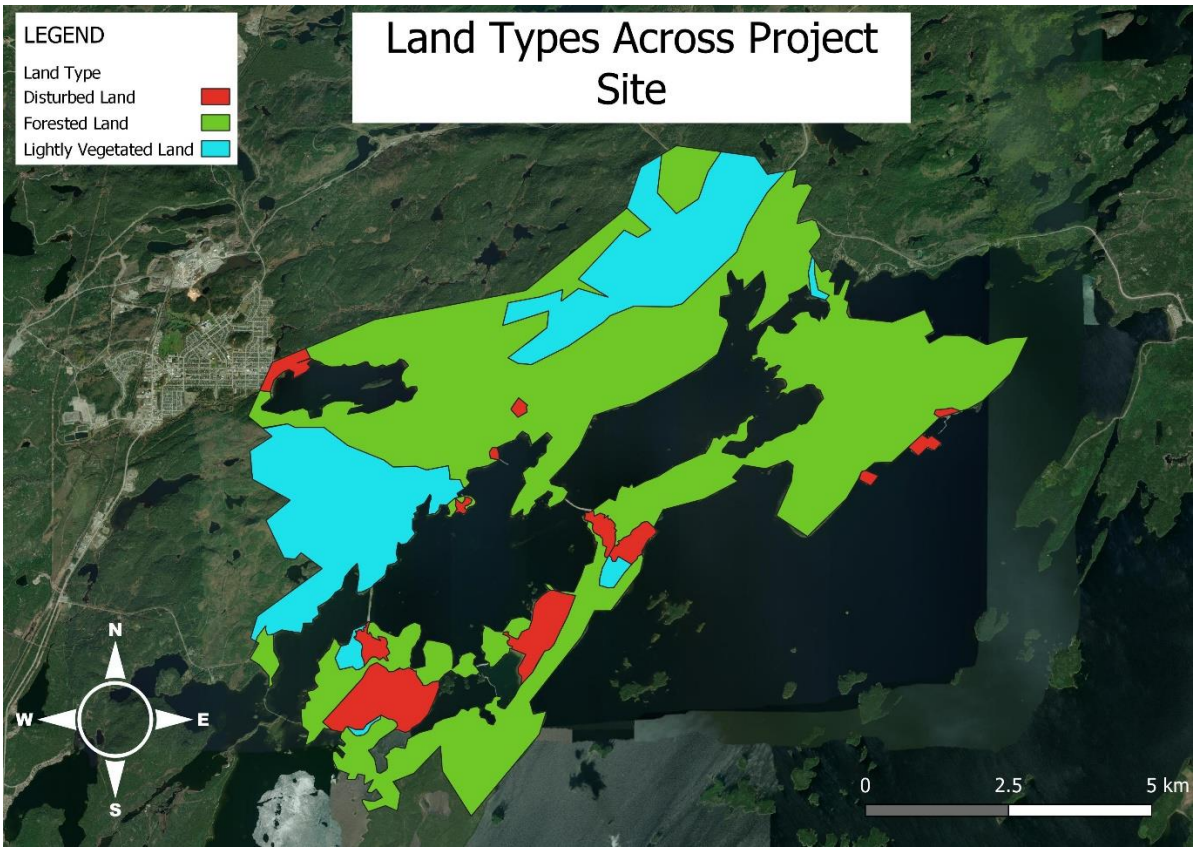


Figure 0.1 - General Landforms Identified Across Study Site (Basemap modified from ESRI Satellite World Imagery)

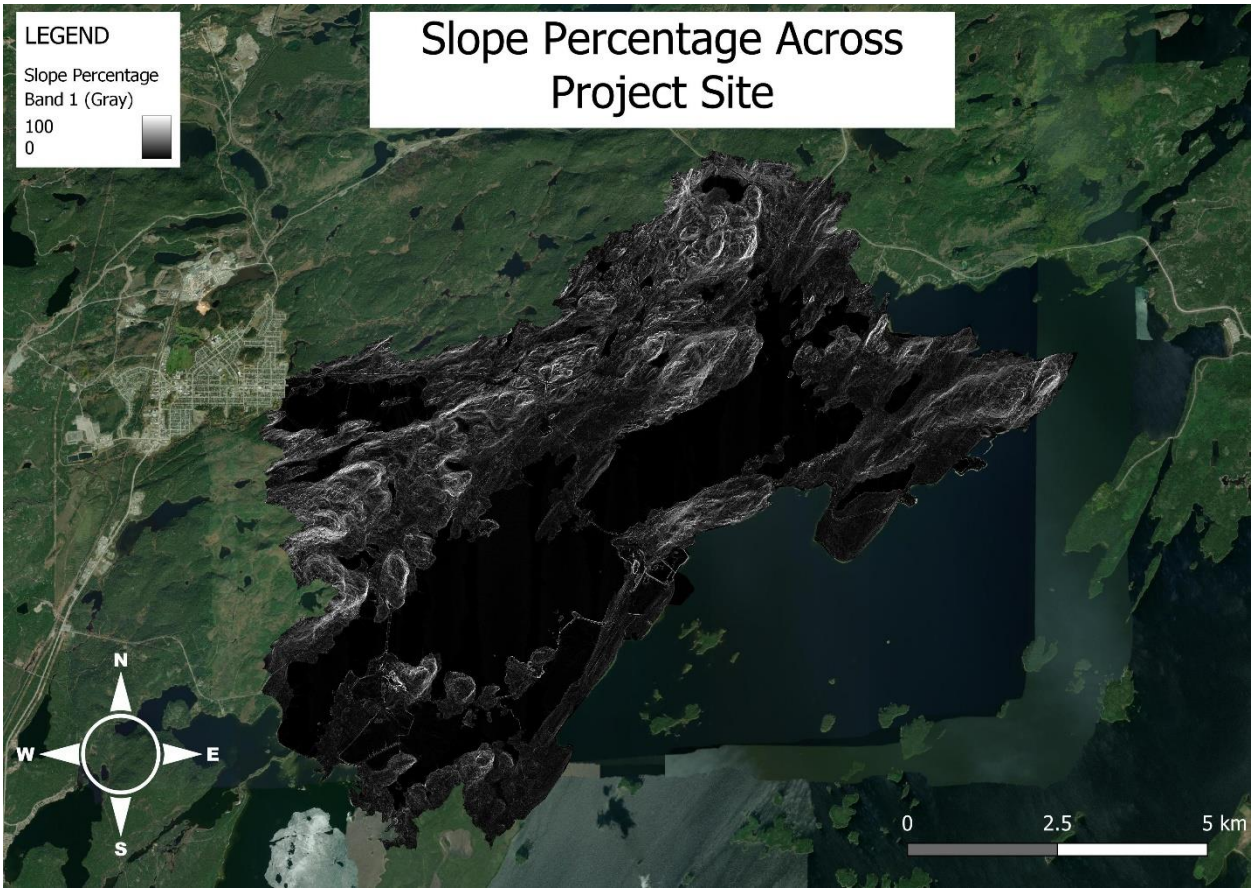


Figure 0.2 - Percent Slope Calculated Across Study Site (Basemap modified from ESRI Satellite World Imagery)

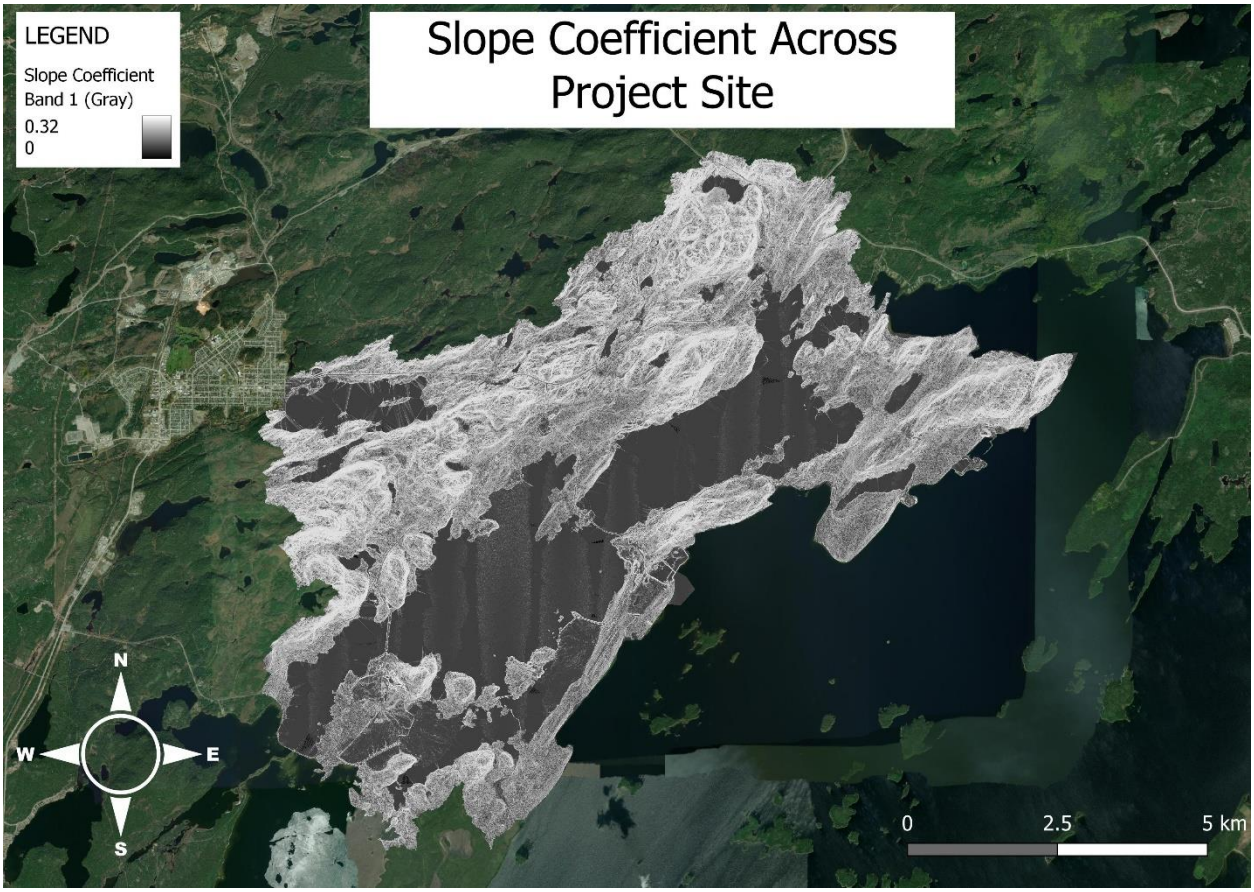


Figure 0.3 - Estimated Slope Coefficient Across Study Site (Basemap modified from ESRI Satellite World Imagery)

For the vegetation factor (Figure A.4), the landmass of the study site was roughly divided into 3 distinct vegetation classes based on visual observation of satellite imagery – Heavy Forest, Light Vegetation, and Disturbed Land. For each class, a vegetation factor coefficient was assigned based the Texas Department of Transportation's Hydraulic Design Manual and a DEM was created with the values of each coefficient corresponding to their land areas (Thomason, 2019).

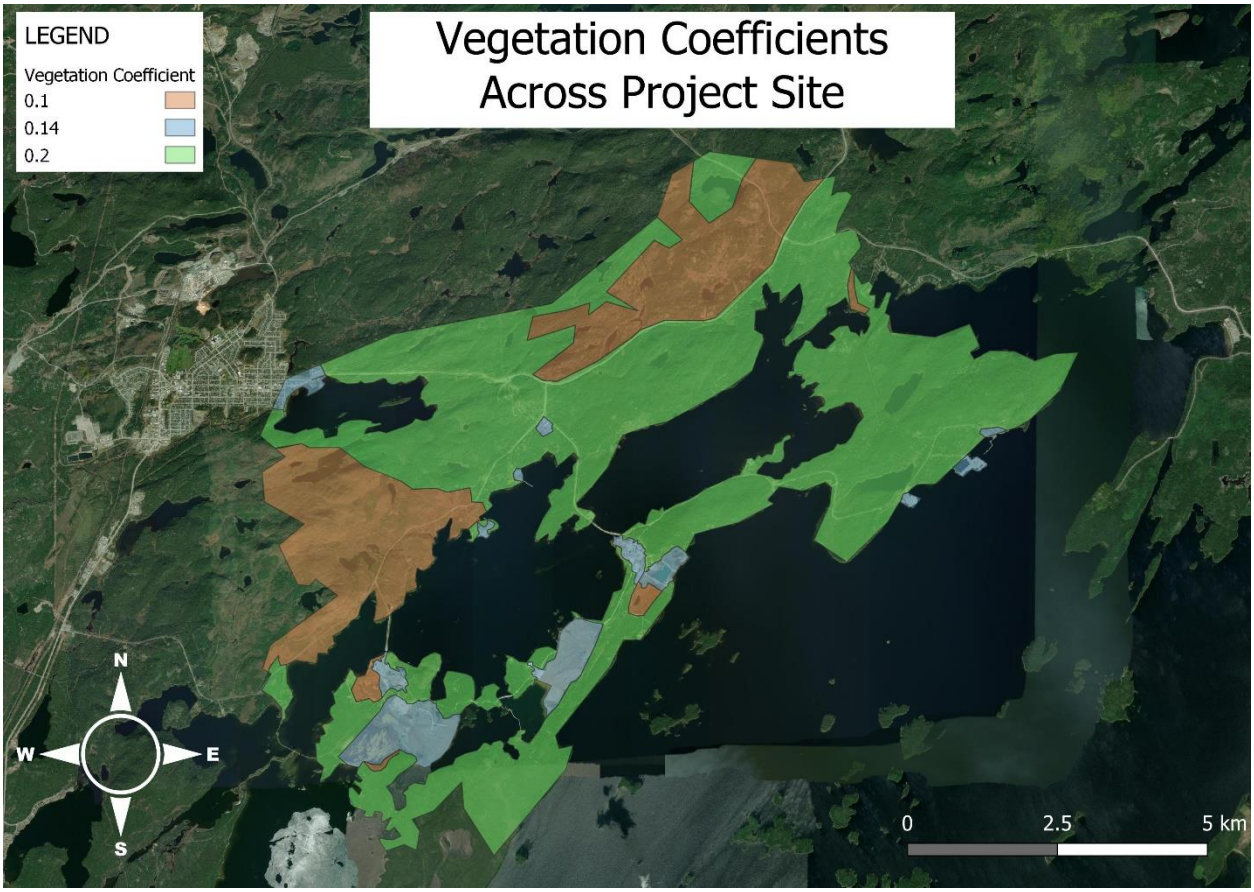


Figure 0.4 - Vegetation Factor Across Study Site (Basemap modified from ESRI Satellite World Imagery)

Based on Quaternary Geology reports for Chibougamau, borehole logs and field excursions to the area, the soil conditions at the site are assumed to be relatively uniform (Martineau, 1984). Soil throughout the study domain is comprised of a thin glacial till lens (<20m), where sediments are mainly fine silts with trace gravels. Thus, a uniform soil factor coefficient (Figure A.5) was assigned based on the Texas Department of Transportation's Hydraulic Design Manual and a constant value DEM was created for this (Thomason, 2019).

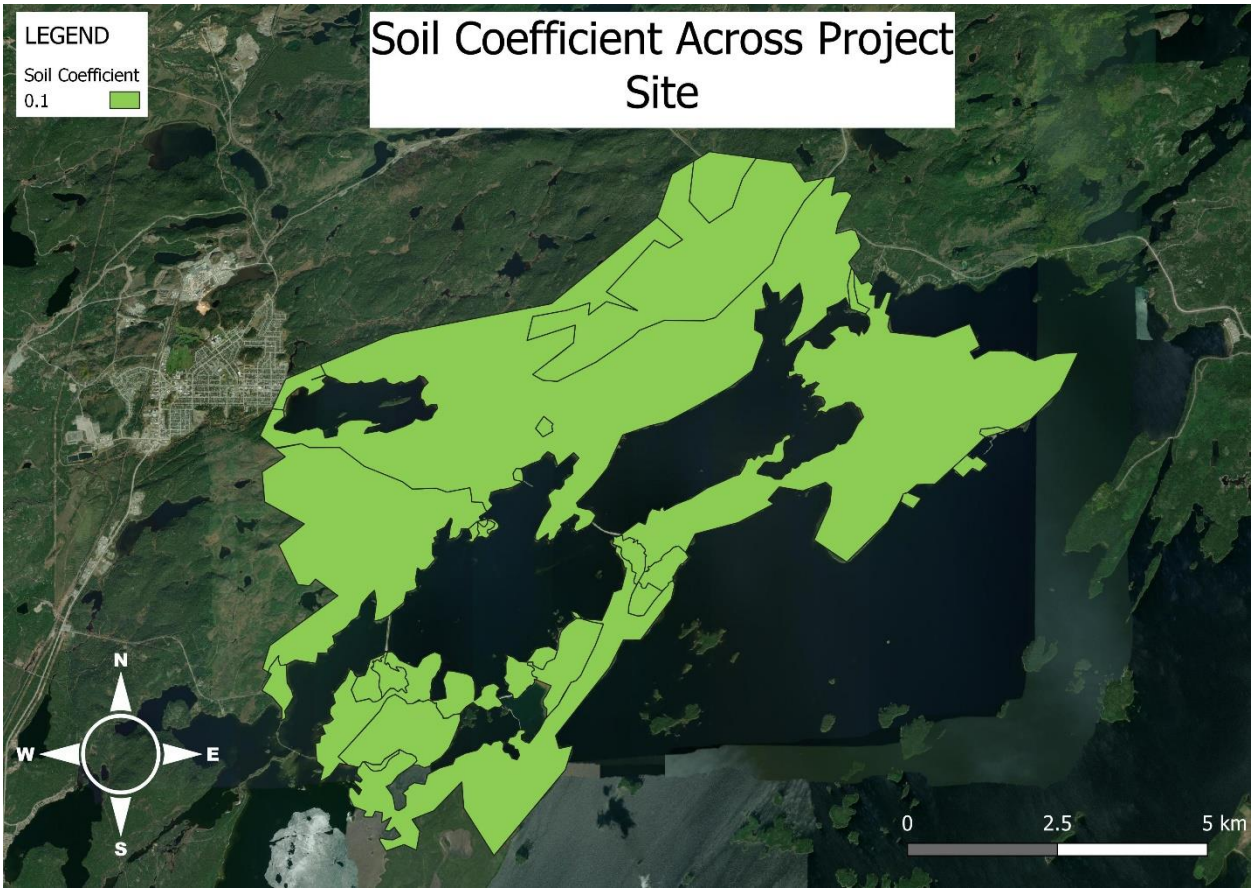


Figure 0.5 - Soil Moisture Storage Coefficient Across Study Site (Basemap modified from ESRI Satellite World Imagery)

With all three coefficients parameterized within DEMs of similar resolution, the raster calculator function in QGIS (QGIS.org, 2022) was used to add them into a resulting DEM that represents the total runoff coefficient discretely across the study site (Figure A.6). All discrete values in the final DEM were averaged to determine the sitewide runoff coefficient of 0.47.

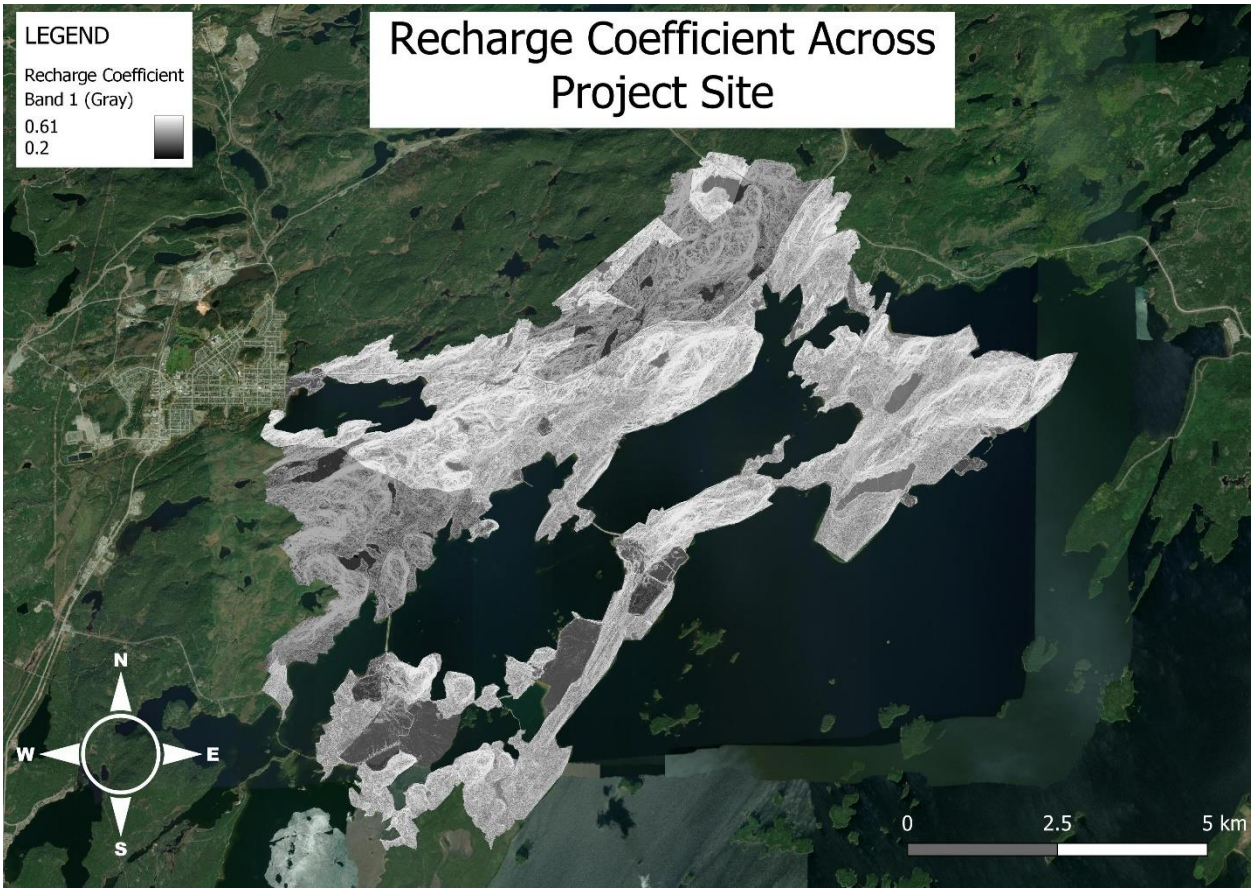


Figure 0.6 - Calculated Recharge Coefficient Across Study Site (Basemap modified from ESRI Satellite World Imagery)

Finally, the precipitation, evapotranspiration, and runoff coefficient were substituted into the following equation for recharge to determine a site wide yearly recharge value (Equation A.9):

Equation 0.9 - Recharge

$$R = P - (ET + Ro + S)$$

Where:

R = Groundwater Recharge (mm/a)

P = Total Precipitation (mm/a)

ET = Actual Evapotranspiration (mm/a)

Ro = Total Runoff (mm/a)

S = Soil Moisture Retention (mm/a)

Note that this methodology appears to have an increasing degree of uncertainty as steeper slopes are introduced into the overall domain, since the upper slope percentages must be reclassified in larger intervals over the same available estimates of slope factor coefficient. Further, this estimate of recharge assumes that precipitation and evapotranspiration measurements are uniform throughout the entire study site and vadose zone composition is relatively homogenous.

For determining ET from CMIP5 data, the Hargreaves-Samani equation is used to calculate an estimate (Shahidian et. al, 2012; Equation A.10).

Equation 0.10 - Hargreaves Samani Estimate of ET

$$ET_0 = 0.0023(T + 17.78)(T_{max} - T_{min})^{0.5} R_a$$

Where:

ET_0 = Potential Evapotranspiration (mm/month)

T = Monthly Mean Temperature (°C)

T_{max} = Monthly Maximum Temperature (°C)

T_{min} = Monthly Minimum Temperature (°C)

R_a = Extraterrestrial Radiation (mm/month)

Appendix C: FEFLOW Governing Equations

Saturated steady-state flow in FEFLOW is solved via the Darcy equation (Equation A.11) for groundwater flow at each node (Diersch Hans-Jörg, 2016):

Equation 0.11 - Darcy's Law

$$q = -K \cdot \nabla h$$

Where:

q = Fluid Flux ($L\ t^{-1}$)

K = Saturated Hydraulic Conductivity ($L\ t^{-1}$)

∇h=Three-Dimensional Hydraulic Gradient (Dimensionless)

Discrete fracture elements in FEFLOW may be represented by three possible relations (Diersch Hans-Jörg, 2016):

1. Darcy's Equation, like the matrix.
2. Hagen–Poiseuille equation, which calculates the pressure drop for an incompressible Newtonian fluid travelling through a long cylindrical channel with constant cross-section.
3. The Manning-Strickler equation, which calculates the velocity of a fluid travelling in an open channel.

The Manning-Stricker formulation is clearly unsuitable for fractures as its applicable to open channels, leaving the modeller the choice of Darcy or Hagen–Poiseuille (Rapantova et. al, 2007). Since a geologic fracture is unlikely to be well modelled by a constant circular cross

section, and available field observation make hydraulic conductivity of the fractures easier to parameterize than aperture size, the Darcy equation is utilized to represent flow through the fractures in the model. Note however that all three formulations require the unlikely assumption that flow through fractures is laminar, thus neglecting turbulent flow effects in these conduits that may arise from partial infill and variances in fracture aperture.

Appendix D: Catchment Analysis

The large-scale regional catchment analysis required for the domain is conducted by a process outlined by Hans van der Kwast (2021) using QGIS (QGIS.org, 2022) with algorithms from the PCRasterTools plugin (Karssenberg et. al, 2010) and digital elevation models (DEMs) sourced from the Government of Québec's Forêt Ouverte spatial database portal (Ministère des Forêts, de la Faune et des Parcs, 2019). The methodology is as follows:

1. Convert DEM to PCRaster format (.map) using the "Convert to PCRaster Format" tool, with output data type set to Scalar.
2. Use the "lddcreate' tool with the output from step 1 as the input file and the default settings to generate a local drainage direction map.
3. Use the streamorder tool with the output from step 2 as the input file to generate a stream network map with Strahler orders.
4. Overlay the output from step 3 onto a map of the site with major streams and manually remove strahler orders so that the streams in the raster file are calibrated to the actual locations of major streams on the map.
5. Use the "lookup table from RAT' tool to generate a table of calibrated strahler order values
6. Use the "lookup" tool with the table from step 5 and the raster file from step 4 as inputs to generate a map of Strahler channels.
7. Use the "downstream" tool with the local drainage direction map from step 2 and the raster from step 6 as inputs to generate a raster of downstream locations.

8. Using the raster calculator, generate a raster file where values from the raster generated in step 6 are not equal to values from the raster generated in step 7 (i.e. strahler channels != downstream) to create a raster map of junction locations. Use "Convert to PCRaster Format" again to convert the resulting raster to PCRaster format (.map) with data type set to Ordinal.
9. Use the "uniqueid" tool with the junctions raster as an input to generate a version of this raster where each junction location is uniquely valued.
10. Use the "convert layer data type" tool to convert the raster data type from step 9 to nominal.
11. Use the "spatial" tool to create a nominal zero map.
12. Finally, use the "catchment" tool with the local drainage direction map from step 2 and the outlet raster from step 11 as inputs to generate the catchments for the study site.

Appendix E: Packer Test Results

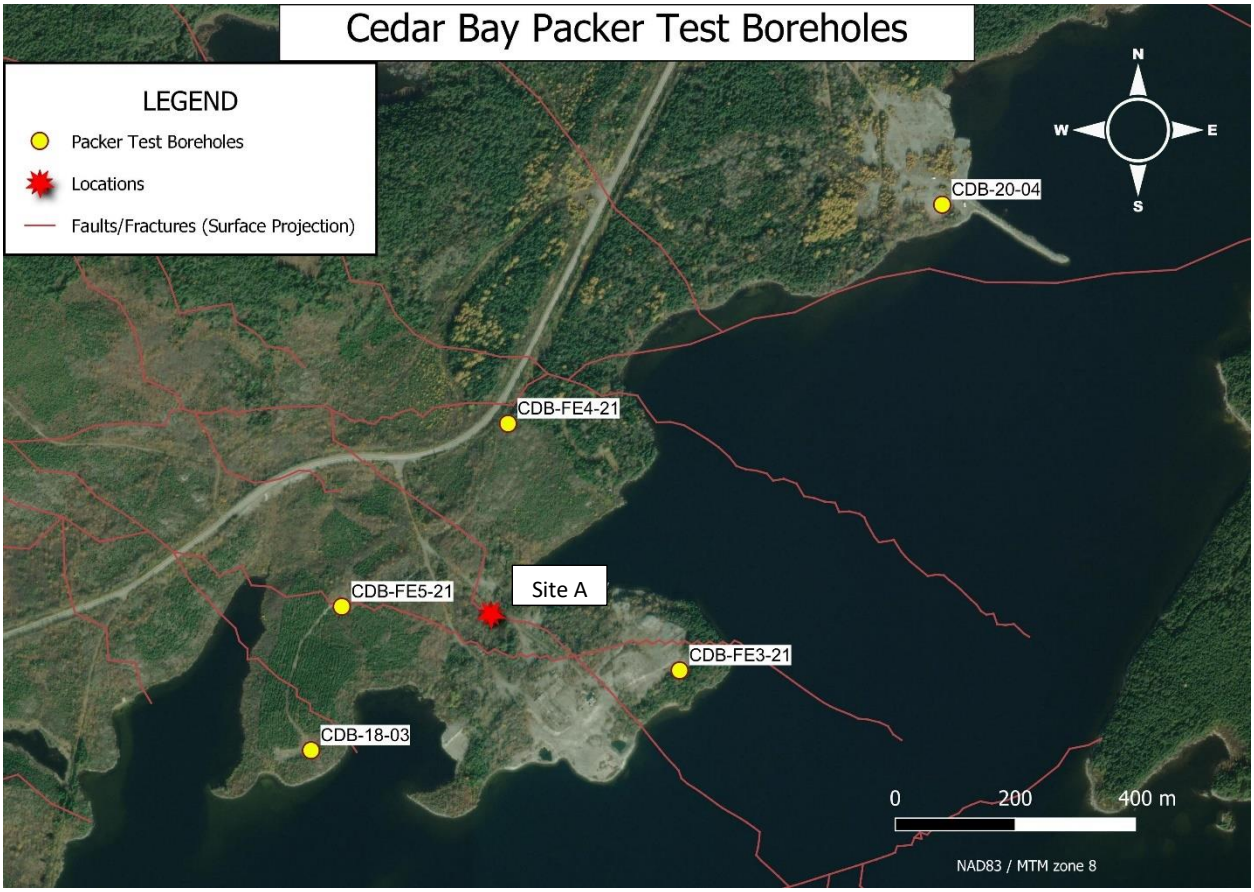


Figure 0.7 - Location of Packer Testing Boreholes (Basemap modified from ESRI Satellite World Imagery)

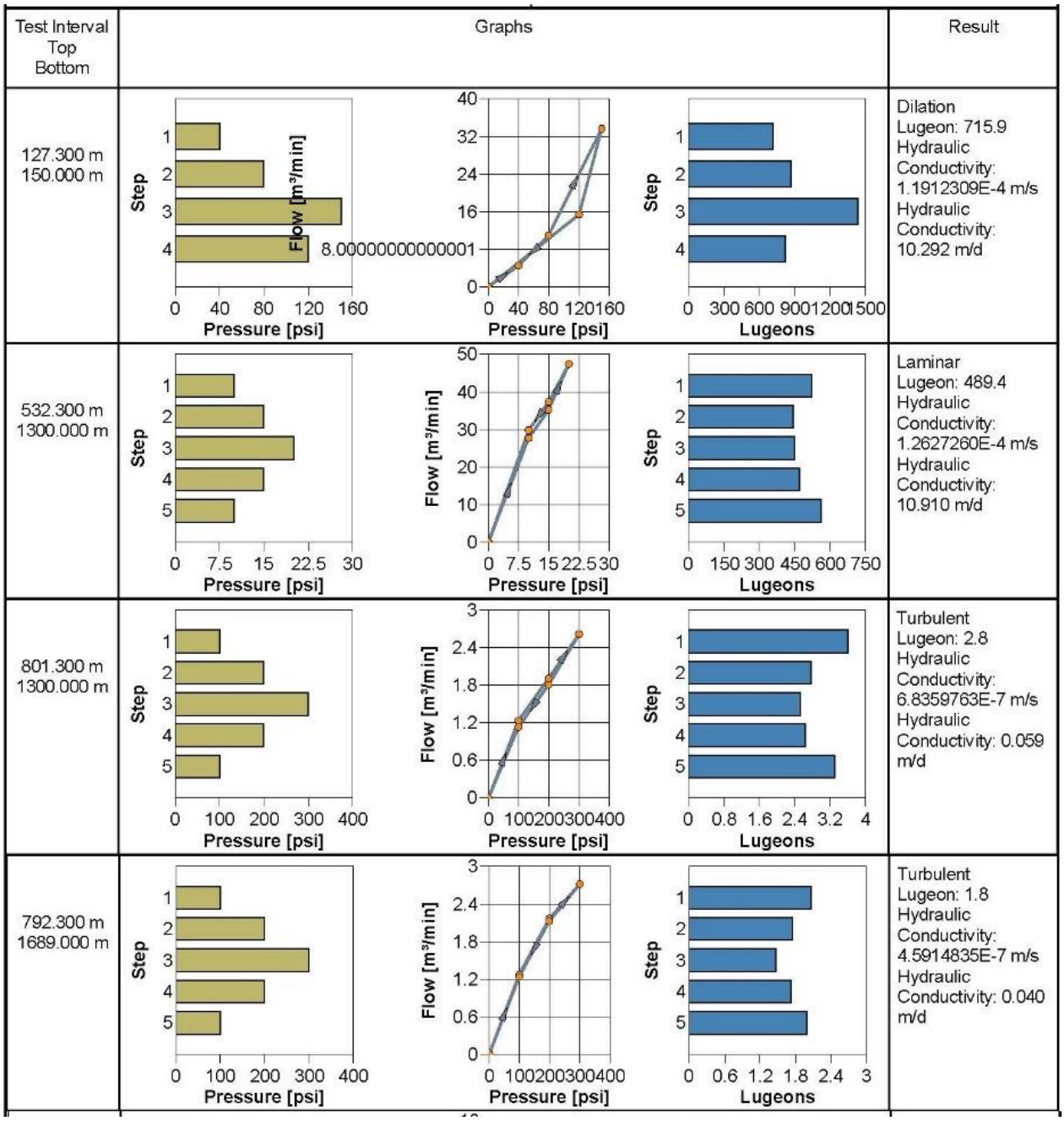


Figure 0.8 - Packer Testing Results (From Top to Bottom – CDB-FE3-21, CDB-18-03 (768m Interval), CDB-18-03 (499m Interval), CDB-20-04)

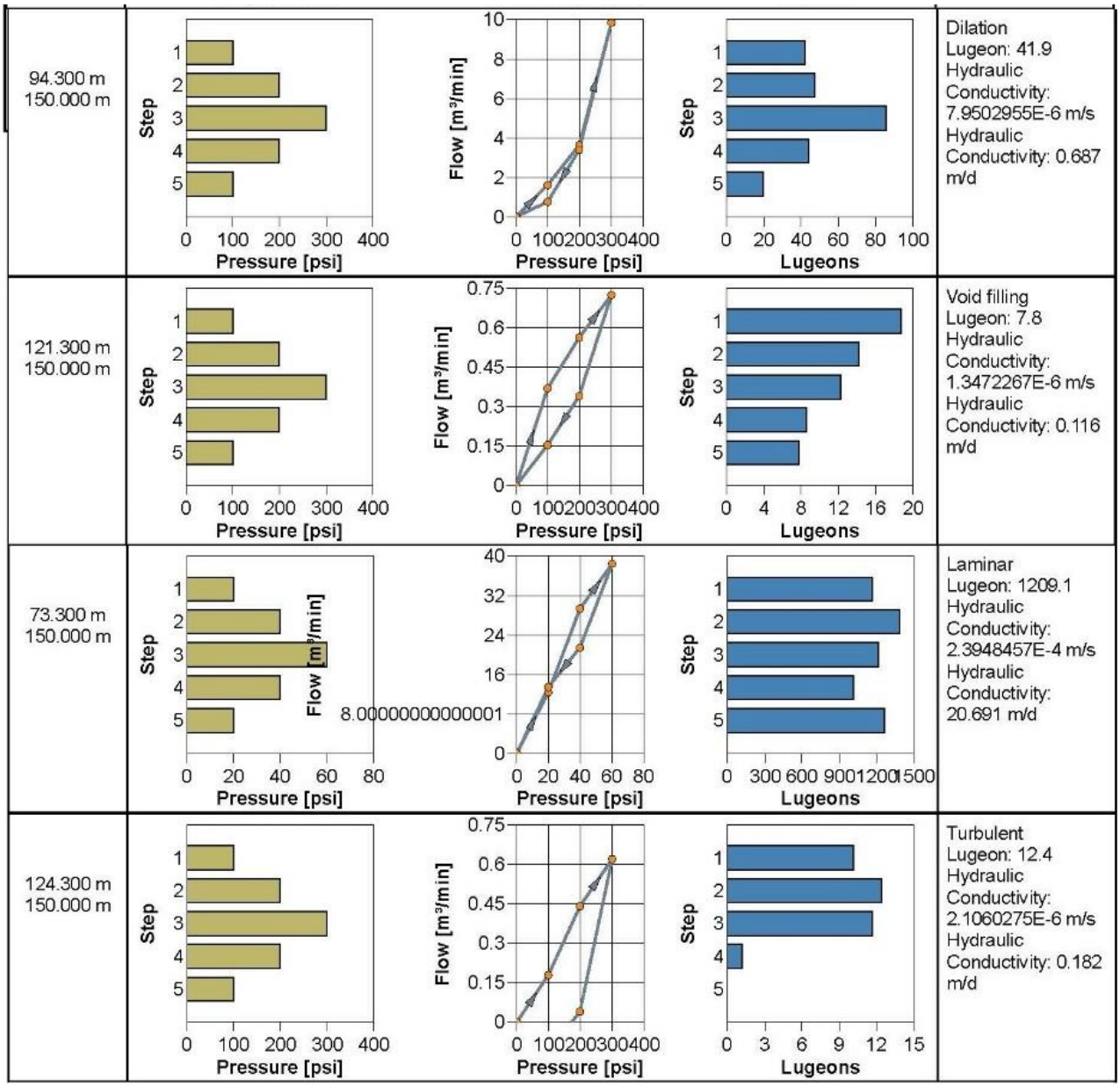


Figure 0.9 - Packer Testing Results (From Top to Bottom – CDB-FE4-21 (56m Interval), CDB-FE4-21 (29m Interval), CDB-FE5-21 (77m Interval), CDB-FE5-21 (26m Interval))

Appendix F: Location and Representation of Galleries

To determine the potential vertical location of the galleries used information from historical records, gathered from technical exploration reports which indicate the maximum historical depth of mining operations – 670.56 metres below surface for Site A (corresponding to a depth in metres above sea level of approximately -290) and 1478.28 metres below surface for Site B (corresponding to a depth in metres above sea level of approximately -1090) (Evans, 2019). Based on current exploration estimates, maximum depth of extraction for Site A and Site B will be 1524m below surface and 1600m below surface, respectively (RadonEx Ltd., 2011).

It is difficult to discern a minimum depth, though the shallowest ore zone of record for Site B is at 487.68 metres below the surface (approximately -100 masl) (Evans, 2019). At Site A, two shafts were sunk – an exploration shaft 159m below surface, and a production shaft as deep as 1036m below surface (Evans, 2019). It may be assumed that galleries can at any level up to the level of the highly competent, near-surface diabase dykes, where economic mineralization is highly unlikely to have existed.

Thus, accounting for the 25m vertical discretization of the model domain, galleries may be modelled anywhere within the following vertical limits:

- Site A Galleries: 220 masl to -1140 masl
- Site B Galleries: -100 masl to -1220 masl

Underground mine dewatering is typically conducted in discrete intervals throughout the depth of the ore body, separated at various levels by a network of shafts. Though a range of

potential mine workers is identified, it is unlikely that economic mineralization occurs at every interval in between. Thus, dewatering may be applied to the model at an arbitrary 100 m interval. In reality, dewatering requirements and efficacy can be assessed on a per level basis by shifting this 100 m gallery section to various depths in the model. For this study, the galleries will be modelled exactly halfway between the minimum and maximum depths over a 100 m vertical extent. Thus, the galleries in the model will exist at approximately the following depths:

- Site A Galleries: -398m to -498m
- Site B Galleries: -698m to -798m

When dewatering is applied to the simulation, the nodes corresponding to locations of the galleries will be assigned a maximum flow constraint constant head boundary, ensuring that they always remain empty during the simulation. When running simulations with dewatering, a constant head boundary with a maximum flow constraint was applied to each node which represented the location of underground galleries, at each slice representing a depth where galleries were considered to already exist or are planned to exist.

Appendix G: Summary of Simulation Results

Table 0.1 - Collective Simulation Results of All Base Case Scenarios

ID	Observed Head (m)	Simulated Heads (m)			
		Base Case - Steady State Saturated - FEFLOW	Base Case - Steady State Saturated - HGS	Transient Unsaturated - 50 Years - HGS	Transient Fully Coupled - 50 Years - HGS
CDB-18-01	381.58	376.25	376.23	376.75	380.23
CDB-20-04	379.74	379.30	377.92	377.99	372.20
CDB-20-05	378.50	378.91	377.92	377.99	372.20
CDB-20-07	380.44	386.67	388.56	386.28	381.12
CDB-20-08	379.19	376.23	376.22	376.68	378.93
CRND-21-01	385.40	402.39	406.04	402.72	388.00
CRND-21-03	412.21	408.46	406.11	408.24	420.17
CRND-21-04	415.77	412.88	411.79	413.83	425.95
CRND-21-05	417.29	413.40	412.04	413.98	423.48
CRND-21-06	412.08	415.56	413.63	415.31	421.07
CR-FE1-21	385.61	409.98	407.32	408.11	386.55
CR-FE2B-21	385.56	412.04	410.14	411.25	393.60
CR-FE3-21	402.48	412.00	411.05	412.87	405.29
CR-FE4-21	376.73	389.70	389.97	390.77	383.67
CR-FE5-21	387.23	394.50	390.94	392.66	395.51

Appendix H: Differences Between Common Node and Dual Node Scheme

Table 0.2 - Summary of Dewatering Rates

Summary of Dewatering Rates - Dual Node Vs. Common Node in FEFLOW (m^3/day)		
Model Case	FEFLOW - Steady State Saturated - Common Node Fractures	FEFLOW - Steady State Saturated - Dual Node Fractures
Site A Galleries	-10774.55	-2891.64
Site B Galleries	-18895.07	-5411.664
Total	-29669.62	-8303.30
Difference Between Common Node and Dual Node:		-21366.32